Metallicity-Dependent Galactic Isotopic Decomposition for Nucleosynthesis

Christopher West[1,3]

west0482@umn.edu

and

Alexander Heger[1,2,3]

alexander.heger@monash.edu

[1]Minnesota Institute for Astrophysics

School of Physics and Astronomy, University of Minnesota

[2]Monash Centre for Astrophysics

School of Mathematical Sciences, Monash University

[3]Joint Institute for Nuclear Astrophysics

Abstract

All stellar evolution models for nucleosynthesis require an initial *isotopic* abundance set to use as a starting point. Generally, our knowledge of isotopic abundances of stars is fairly incomplete except for the Sun. We present a first model for a complete average isotopic decomposition as a function of metallicity. Our model is based on the underlying nuclear astrophysics processes, and is fitted to observational data, rather than traditional forward galactic chemical evolution modeling which integrates stellar yields beginning from big bang nucleosynthesis. We first decompose the isotopic solar abundance pattern into contributions from astrophysical sources. Each contribution is then assumed to scale as a function of metallicity. The resulting total isotopic abundances are summed into elemental abundances and fitted to available halo and disk stellar data to constrain the model's free parameter values. This procedure allows us to use available elemental observational data to reconstruct and constrain both the much needed complete isotopic evolution that is not accessible to current observations, and the underlying astrophysical processes. As an example, our model finds a best fit for Type Ia contributing $\simeq .7$ to the solar Fe abundance, and Type Ia onset occurring at $[\text{Fe/H}] \simeq -1.1$, in agreement with typical values.

Subject headings: Galaxy: evolution, Galaxy: abundances, stars: abundances, nucleosynthesis, (stars:) supernovae

1. Introduction

Yields from stellar simulations depend on the initial isotopic composition of the star. For example, the initial composition is important during hydrostatic burning phases for neutron capture reactions on initial metals, affecting odd-z nuclei abundances. In massive stars the weak s-process yields are constrained by both the initial CNO abundance, which is responsible for providing a neutron source, and also the initial Fe abundance which supplies the seeds for neutron capture (Pignatari et al. 2010). The initial Fe abundance is also important in intermediate and low-mass asymptotic giant branch (AGB) stars for seeding the main s-process yields (Käppeler et al. 1989, 2010; Lattanzio and Lugaro 2005). The detailed stellar abundances affect the opacity of the star (e.g., the The Opacity Project 1995), which in turn will affect the structure as well as mass and angular momentum loss, which in turn changes the late stellar evolution. Knowing the initial abundances of heavy isotopes is crucial for understanding γ-process abundances, which use s- and r-process isotopes as seeds (Rauscher et al. 2002; Arnould and Goriely 2003). Since these p-isotopes are so rare, any difference in the seed abundances propagates to the resulting γ-process yields. Finally, some fraction of the initial stellar composition is not processed and will return to the interstellar medium (ISM) unchanged, hence the final abundance pattern will directly inherit any poorly estimated initial abundances, but in many cases what is made in the stars and what was there initially is difficult to disentangle.

The purpose of galactic chemical evolution (GCE) is to understand how the abundances of the elements and their isotopes evolved from the Big Bang to today, and can be used for obtaining the isotopic abundances at any metallicity to use as stellar simulation inputs. Traditional GCE models typically split a model galaxy into one or more zones that require functional forms for infall and star formation rates (Timmes et al. 1995; Chiappini et al. 1997; Costa et al. 2009; Henry et al. 2010). Other processes such as interstellar medium

(ISM) mixing, and galaxy mergers are often not addressed, although there have been fairly recent efforts to incorporate mergers in a hierarchical model (Tumlinson 2006). The model galaxy is then usually evolved by integrating stellar yields over time, hence these models require nucleosynthesis yields from stellar simulations as inputs. The difficulty with this approach is that in order to provide self-consistent nucleosynthesis yields, the stellar simulations need a complete initial set of isotopic abundances.

Ideally, such a set would come directly from the GCE simulation. This would require knowledge of the complete set of stellar yields for the specific abundances of the GCE model at each time step and for each zone: the complicating factor is in reality composition is *not* just a function of metallicity, but also a function of environment, i.e., time and space. Instead the inputs for the stellar simulations often use scaled solar abundances or the results of some other approximation. Furthermore most GCE models usually evolve only a subset of the stable isotopes, such as just the iron peak isotopes (Henry et al. 2010) or everything from hydrogen up to the iron peak (Timmes et al. 1995; Kobayashi et al. 2006), or only elements. An approach different than GCE modeling to describe chemical abundances has been done recently by Ting et al. (2012). They perform a principle component analysis on elemental data that takes correlations among elemental ratios and roughly delineates different processes responsible for these correlations, as well as identify likely sites and metallicity regimes congruent with them. These efforts offer verification of the established paradigm concerning many astrophysical processes, and may help constrain others whose properties remain incompletely known.

The approach taken here is complementary to traditional GCE methods, however, one must take care not to confuse our model with a proper GCE model. We construct an astrophysical model of all stable isotopes, based on physical principles for the production sites and mechanisms. Effectively, we scale isotopic abundances as a function of a chosen

model parameter. This isotopic model is then mapped to an elemental model by summing the isotopic abundances to their respective elements. We then fit the elemental abundances against available observational data to obtain numerical values for the free parameters of the model. Our completed model then gives the average *isotopic* history of the Galaxy, subject to the approximations employed. The benefit of this approach to isotopic GCE is that it is not necessary to know or model dynamic and galactic evolution processes employed in traditional GCE models such as infall, ISM mixing, and galaxy mergers, whose uncertainties are poorly constrained.

Compared to full GCE calculations our approach is rather simplistic and approximate, precisely because we do not integrate stellar yields or address dynamic and galactic evolution processes employed in traditional GCE models, and we assume a unique and *typical* abundance distribution for a given metallicity rather than allowing for a spread in distribution as found in nature. The intention here is to improve upon the typical standard of scaling isotopic solar abundances by a constant factor, which effectively treats all isotopic production as primary. Our improvements to this standard is to incorporate secondary processes and Type Ia contributions with separate scalings, to better approximate their relative values at desired input metallicities for nucleosynthesis studies, and the resulting isotopic histories from our model can be used as inputs in stellar models, and comparison to abundances from other sources like Damped Lyman-α systems and dwarf galaxies. This represents an improvement over the previous standard of guessing *ad-hoc* assumptions for the interpolation between the known endpoints of solar and big bang nucleosynthesis (BBN), or the use of scaled solar abundances. This model could also be seen as a first iteration step for more sophisticated first principle GCE models, but at a higher order approximation than just scaled solar abundances, but not a replacement for them. Hence, whereas the approximations and comparisons of our model are sufficient for this purpose, they would be quite unsatisfactory for describing GCE itself.

This paper has the following outline: Section 2 introduces the astrophysical processes and sites considered by the model, and the separation of the solar isotopic abundance pattern into contributions from these processes is discussed. In Section 3, the model itself is introduced and the scaling of the processes as a function of our parametrization is explained, using their relative solar contributions and the BBN abundance pattern as fixed boundary conditions. This also defines the relevant free parameters for fitting the elemental abundances with stellar data. In Section 4, the elemental model is fit to available data and best fit parameter values are found. In Section 5, the resulting elemental model is discussed and additional results given by the model. The final Section 6 addresses constraints of the model and discusses possible extensions for future work.

2. Astrophysical Processes and Solar Abundance Decomposition

Our model attempts to cover the essential key astrophysical processes responsible for the production of the isotopes in the Galaxy. We first use these processes to decompose the solar system abundances. Here the isotopic solar abundance pattern was taken from a new data set by Lodders et al. (2009) which gives updated values relative to their 2003 publication (Lodders 2003). In the following we organize the processes roughly by the mass range of isotopes to which they contribute.

2.1. Big-Bang Nucleosynthesis

When the Universe was less than $\sim$100 seconds old, protons and neutrons were in thermal equilibrium with each other by weak interactions with neutrinos. Upon continuing expansion, however, the temperature dropped sufficiently to "freeze out" neutrino interactions. At this "freeze-out" temperature, corresponding to $k_B T \sim 0.8\,\mathrm{MeV}$, the weak

interaction rate became slower than the hubble expansion, and the neutron-to-proton ratio (after some subsequent β decay) was fixed to n/p $\simeq$ 1/7 (Yao et al. 2006). At this point BBN began with deuterium formation, and proceeded to produce non-negligible abundances of ^{2}H,^{3}He, ^{4}He, ^{7}Li, and minute abundances of ^{6}Li and isotopes up through oxygen.

We use the theoretical BBN abundance pattern from Cyburt et al. (2001) and provided by Fields (2002). Isotopic contributions from this BBN pattern are taken for ^{1}H, ^{2}H, ^{3}He, ^{4}He, and ^{7}Li. The remaining negligible contributions of ^{6}Li and the isotopes heavier than ^{7}Li are not used. A constant ^{7}Li abundance at low metallicities has been observed that suggested a primordial abundance, but whose value was much smaller than the predicted BBN abundance (Spite and Spite 1982). This "Spite plateau" remains unexplained, and for the present model we use the theoretical BBN abundance for ^{7}Li.

2.2. Light Isotopes

2.2.1. Helium

The remaining helium not made during BBN is a product of hydrogen burning and is scaled as a primary process. The "release time scale" of helium can vary depending on the stellar mass, and relative to metallicity it may scale slightly slower than a true primary process (the same is true for C and N). We do not account for this delay in the present model.

2.2.2. ν-Process

The "light" ν-process involves interactions among neutrinos and lighter nuclei in CCSNe environments (Woosley et al. 1990; Yoshida et al. 2004; Heger et al. 2005). The neutrinos

elevate nuclei to excited states, which then decay by nucleon emission (Hartmann et al. 1991). The target nuclei for these interactions that produce light isotopes are CNO isotopes made from hydrogen and helium, hence this production is primary. This process produces ^{11}B (Heger et al. 2003), and some ^{7}Li (Prantzos 2010). The "heavy" ν-process also involves neutrino interactions, but with target nuclei made from either the s- or r-processes, and is responsible for heavy nuclei production such as ^{180}Ta and ^{138}La. Due to the requirement of pre-existing s- or r-process metals to serve as the target nuclei, the "heavy" ν-process behaves like the γ-process with respect to metallicity, discussed below in Section 2.5.6. Hence we do not distinguish between the "heavy" ν-process and γ-process contributions. In our model, the ν-process stands for the "light" ν-process, and the γ-process includes the "heavy" ν-process.

2.2.3. Galactic Cosmic Ray Spallation

Galactic Cosmic Ray (GCR) spallation events occur when energetic protons or α-particles impact on existing CNO nuclei in the ISM (Reeves et al. 1970; Meneguzzi et al. 1971). GCR spallation contributes to ^{6}Li, ^{9}Be, ^{10}B, and ^{11}B (Prantzos 2007, 2010). Since spallation occurs on pre-existing CNO nuclei in the ISM, this process is traditionally considered secondary. Observations, however, show a primary dependence on metallicity for ^{9}Be (Prantzos 2007), which is in conflict with the understanding of spallation events. Prantzos (2012) and Prantzos (2010) proposes a solution to this problem, and states that GCRs accelerated by the winds of rotating massive stars could be abundant in CNO isotopes. If these GCRs then hit ISM protons or α-particles, this would satisfy the condition of a primary event. We adopt this proposed solution, and assign primary GCR spallation as a mechanism for LiBeB production, along with secondary GCR spallation (Prantzos 2007, 2010, 2012).

2.2.4.   Classical Novae

White dwarfs accreting material from a companion star can undergo outbursts powered by thermonuclear runaway in the accreted layer (Truran 2002; José and Hernanz 2008). Nucleosynthesis occurs on the accreted material that is rich in H and He and dredge-up of primary CNO (and ONeMg for ONeMg novae) into the envelope, hence this process is primary. Unlike most other primary processes that immediately begin to enrich the ISM however, there is likely some onset timescale for novae contributions similar to Type Ia SNe. We do not consider this delay for novae in our model. Simulations have shown differing isotopic production below the iron peak, depending on the composition of the core and its mass (Gehrz et al. 1998; José and Hernanz 2007, 2008). Hence precise abundance determinations are difficult to isolate. Many CO novae simulations show production of ^{7}Li, ^{13}C, ^{15}N, ^{17}O, and ^{19}F that dominate the ejecta, whereas ONeMg novae additionally show contributions to other metals up to ^{40}K (José and Hernanz 2007). We take all contributions beyond ^{7}Li to be negligible compared to massive star contributions. This approximation holds well for CNO isotopes that have large contributions from massive stars, but for isotopes such as ^{19}F the approximation is less than ideal. In fact it believed that ^{19}F may also be produced in the ν-process in core-collapse supernovae (CCSNe; Woosley and Haxton 1988), during hydrostatic nucleosynthesis in He shell of thermally pulsating asymptotic giant branch stars (TP-AGB; Forestini et al. 1992), and in the He core of heavy mass loss Wolf-Rayet stars (Meynet and Arnould 2000). The decomposition from these sources is still a matter of debate (Abia et al. 2010; and references therein), and we do not address this complication in the current model.

2.2.5. Light Isotope Decomposition

Identifying the precise (non-BBN) Li, Be, and B contributions presents a challenge. At present, there is no consensus for explaining the solar abundance pattern for the isotopes of these elements using the processes that could be responsible. Due to the difficulty in determining what fraction each actually contributes to the light isotope solar abundance pattern, novae, the ν-process, and primary GCR spallation are placed into a single category due to their shared primary nature. Standard GCR spallation is treated separately since it is secondary. The relative solar abundance decomposition between these two categories for ^{6,7}Li, ^{9}Be, and ^{10,11}B is estimated from Prantzos (2012). Both Li isotopes are given $\approx 30\%$ secondary contributions, and the ^{9}Be, and ^{10,11}B isotopes are given 25% secondary contributions. The remaining non-BBN contributions for all LiBeB isotopes are assigned the novae/ν-process/primary GCR spallation category. Note the decomposition for these light isotopes are at best known to within $\approx 5\%$.

2.3. Low and Intermediate-Mass Stars

Stellar winds from low and intermediate-mass stars are rich in C and N isotopes (Arnould et al. 2003), and provide significant contributions to the solar abundances for these isotopes. Fitting the contributions from these sources to data is problematic, since contamination from massive stars is always present and difficult to separate out. Hence we do not independently address stellar wind contributions in our model and instead combine their contributions with those of massive stars, both of which are primary processes.

2.4.   Intermediate-Mass and Iron Group Isotopes

Hydrostatic burning in massive stars ($\sim 10 - 100\,\mathrm{M}_\odot$) synthesizes most isotopes from helium up to the iron peak (Burbidge et al. 1957; Rauscher et al. 2002). Stellar winds can eject some of this material over the star's life but the explosive stellar death dominates the metal yields. CCSNe likely produces between $1/3$ and $2/3$ of the solar abundance iron peak isotopes (Timmes et al. 1995). They also produce the majority of the alpha isotopes and many of the intermediate isotopes from ^{16}O to the iron group. Type Ia SNe are thermonuclear explosions of accreting white dwarfs (eg., Nomoto et al. 1997; Hillebrandt et al. 2000; Woosley 2001), and primarily provides the remaining iron peak solar abundances, with some enrichment of other metals (Travaglio et al. 2004b; Maeda et al. 2010). In fact, simulations show Type Ia production of minute trace contributions to the isotopes below the iron peak (Nomoto et al. 1997), with the exception of ^{40}K. Both CCSNe and Type Ia produce their isotopic yields explosively, which destroys much of the initial metal composition. The evolutions of their isotopic products are considered primary.

Yields for Type Ia supernovae were taken from the W7 model (Nomoto et al. 1997) for isotopes with mass numbers $12 \leq A \leq 56$. The category of "massive star contributions" is defined in this context to be the collection of all primary isotopic production with mass numbers $12 \leq A \leq 68$ not attributed to Type Ia SNe. This includes all isotopic enrichment to the ISM driven by massive star stellar winds and production from CCSNe, the r-process, the ν-process, novae yields, and stellar winds from low and intermediate-mass stars, with production from CCSNe dominating the isotopic abundances in this category. The solar contributions from massive stars were taken from the yields of a massive star simulation (Heger and Woosley 2010) fitted to stars in the range $-3.1 \leq [\mathrm{Fe/H}] \leq -2.9$ from the Frebel (2010) data set. We use the common definition: $[\mathrm{X}] \equiv \mathrm{Log}(\mathrm{X/X}_\odot)$. Note that the "iron metallicity" (relative to solar), $[\mathrm{Fe/H}]$, should be distinguished from the total metallicity,

[Z]: The former is a conventional proxy for the latter. The simulation included stars in the mass range $10 - 100 \, \mathrm{M_\odot}$, with a Salpeter initial mass function (IMF) and a low mixing of 0.02512 (Joggerst and Heger 2008) employed in a running boxcar method (Heger and Woosley 2010). The explosion energy of the supernovae was set to be $E = 1.2 \, \mathrm{B}$, where $1 \, \mathrm{B} = 10^{51}$ erg.

The fit of the yields to the Frebel (2010) data set gave a χ value of 2.218 (see Heger and Woosley 2010 for fitting procedure). The heavier massive star contributions for mass numbers $57 \leq A \leq 68$ were not taken from Heger and Woosley's massive star simulation, and were instead calculated as residuals from the main and weak s-processes, discussed below in Section 2.5.

Under the assumption that Type Ia are responsible for some fraction f of the observed solar ^{56}Fe abundance, each W7 yield was scaled to this fraction. The scaling factor is given as: $f \cdot X_{56}^\odot / X_{56}^{Ia}$, where $X_{56}^\odot$ is the solar abundance of ^{56}Fe, and X_{56}^{Ia} is the W7 yield for ^{56}Fe. Hence each isotopic abundance was scaled by this factor, which shifts the entire abundance pattern until the yield for ^{56}Fe is equal to $f \cdot X_{56}^\odot$. The fraction f represents a free parameter in the model, which is determined by fitting the elemental scalings against available data (in Section 4). The massive star yields were scaled to the remaining contribution to solar ^{56}Fe not accounted for by Type Ia. This factor is given as: $(1 - f) \cdot X_{56}^\odot / X_{56}^{\mathrm{massive}}$, where $X_{56}^{\mathrm{massive}}$ is the massive star yield for ^{56}Fe. An additional scaling of both types of SNe data in the range $12 \leq A \leq 56$ was then required to ensure that the massive star and Type Ia contributions summed to the solar abundance for every isotope, as the first scaling using f would only guarantee that ^{56}Fe satisfied this requirement. This additional scaling preserved the ratio of each isotopic contribution between the W7 and massive star yields,

$$X_{i,\mathrm{f}}^{\mathrm{massive}} = \left(\frac{X_i^\odot}{X_{i,0}^{\mathrm{massive}} + X_{i,0}^{\mathrm{Ia}}} \right) X_{i,0}^{\mathrm{massive}} \tag{1}$$

$$X_{i,\mathrm{f}}^{\mathrm{Ia}} = \left(\frac{X_i^{\odot}}{X_{i,0}^{\mathrm{massive}} + X_{i,0}^{\mathrm{Ia}}} \right) X_{i,0}^{\mathrm{Ia}} \qquad (2)$$

where $X_{i,0}$, $X_{i,\mathrm{f}}$ are the original and (scaled) fitted abundances of isotope i, for either the massive or Type Ia contributions (denoted as superscripts), and $X_i^{\odot}$ is the solar abundance of isotope i. Note that for clarity this procedure has been explained using two successive scalings, but in practice this can be done with a single scaling that achieves both. This second scaling preserves the isotopic ratios *across* each model, but the ratios *within* each model undergo some distortion. That is, the overall abundance patterns of the W7 and massive star simulations are altered. Nevertheless, the final abundance patterns we use still show Type Ia contributing mostly to the Fe peak, and massive stars contributing to CNO and α-elements up to the Fe peak.

The use of the solar metallicity W7 model is approximate. In our Galaxy, large contributions to the SN Ia yields may come from sub-solar progenitors. The exact nature and properties of these sources, however, are still uncertain (see, for e.g., Bours et al. 2013; Timmes et al. 2003), and given these uncertainties the inclusion of the W7 yields, while not a complete description, is also not unreasonable. To investigate the impact of this approximation, we also computed the solar abundance decomposition for the massive stars and Type Ia using a composition between that of the W7 and W70 models to estimate a sub-solar composition. We then compared the ratios of the isotopes between ^{12}C and ^{56}Fe from our original decomposition and this new one. Of the 53 isotopes in question, 45 have ratios of the new abundance (using sub-solar Type Ia) over the old abundance (solar Type Ia) that are within 2.0. Of the 8 that remain, the largest differences are ^{40}K, which now has a nonzero abundance, and ^{15}N, ^{41}K, ^{43}Ca, and ^{47}Ti, which have ratios of ~ 300, 15, 40, and 20, respectively (the others have ratios within 5). This does present non-trivial corrections to the solar abundance decomposition, but except for a few isotopes, the changes are quite

minor (within a factor of 2). It is unlikely that these changes would noticeably impact the fittings to data we perform later.

2.5. Heavy Isotopes

2.5.1. Weak S-Process

The s-process is one of the four trans-iron processes for making the heavier nuclides distinguished here. It synthesizes isotopes via slow neutron capture (relative to the beta decay rate; Burbidge et al. 1957). It is responsible for approximately half the heavy isotopes beyond iron (Pignatari et al. 2010; Heil et al. 2007). Since this process is characterized by neutron capture rates that are slow compared to the beta decay rate of the target nucleus, production proceeds along the path of isotopic stability, with ^{56}Fe playing the role of the seed nucleus. In practice many metals could seed this process, but ^{56}Fe will stand as the sole target nucleus due to its large abundance and neutron capture cross section relative to other potential seeds. The weak component of the s-process occurs in massive stars, during convective core He burning and shell C burning (Pignatari et al. 2010). The neutron source in core He burning is from the reaction ^{22}Ne(α,n)^{25}Mg. The ^{22}Ne nuclei are produced from the burning of ^{14}N made previously in the CNO cycle. Subsequent C shell burning can produce neutrons by itself and provide α-particles to reignite the ^{22}Ne(α,n)^{25}Mg neutron source. These neutrons are captured on initial ^{56}Fe present in the star.

The weak s-process component can only synthesize isotopes along the line of stability up to a mass number of $A \approx 100$ (Raiteri et al. 1993), due its smaller neutron exposures relative to the main component. Both components of the s-process rely on the existence of metals that formed the initial composition of the star, and therefore are considered secondary processes. The *neutron source* for the main s-process, however, is primary (as

well as some of the shell C burning contributions to the weak s-process), which could result in a behavior between that of a primary and secondary process.

For both the main and the weak components of the s-process, bottlenecks exist at closed neutron shells, allowing the abundances at these corresponding mass numbers to accumulate into peaks. Three such peaks exist at approximate mass numbers 88, 138, and 208. Elements of interest at these peaks for representing the scaling of s-process elements include strontium, barium, and lead. Good recent compilations of the main s-process can be found in Lattanzio and Lugaro (2005), and a good review of the s-process can be found in Käppeler et al. (2010).

Modeling the weak s-process has been less successful than models for the main component (Pignatari et al. 2010). Since flow equilibrium is not reached during the neutron exposure, uncertainties in the neutron capture cross-sections affect the yields of all subsequent isotopes (Heil et al. 2007). We need to reproduce the solar system abundances for the s-only isotopes for both the main and weak components. For the weak s-process, the s-only isotopes ^{70}Ge, ^{76}Se, ^{80}Kr, ^{82}Kr, ^{86}Sr, and ^{87}Sr owe their solar abundances to *both* the main and weak components (Raiteri et al. 1993), and the relative contributions from each represent a poorly known *a priori* constraint. Additionally, recent stellar model calculations for the weak s-process have difficulties in both producing sufficient s-only isotopic yields without at the same time overproducing many other isotopes beyond their solar abundances (Pignatari et al. 2010).

For the purposes of making a reasonable assessment of the weak s-process contributions to the solar system abundances, we performed a calculation using the updated online MACs compilation from the KADoNIS project *www.kadonis.org* (Dillmann et al. 2009). The branching points addressed in our calculation that lie along the weak s-process path are the unstable nuclei ^{64}Cu and ^{80}Br, with corresponding β^+ and β^- thermal branching

ratios calculated from Takahashi et al. (1987). The branching point at ^{79}Se was ignored, and was taken via β^- decay to ^{79}Br prior to any neutron capture (which would give a ^{80}Se population). This approximation is due to the high temperature dependence of the β^- decay rate of ^{79}Se (Heil et al. 2008; Makinaga et al. 2009; Walter et al. 1986). ^{93}Zr was treated as stable for this calculation, since the thermal β^- decay branching ratio is small relative to neutron capture rate (Takahashi et al. 1987). After the neutron exposure has ended, the remaining ^{93}Zr abundance is taken to ^{93}Nb. The ^{85}Rb branching was omitted and it was assumed that it entirely β^- decays to ^{86}Sr, again because the neutron capture branching ratio is negligible (Takahashi et al. 1987).

The differential equations for the weak s-process abundances under the classical approximation (Käppeler et al. 2010) were solved numerically. We have the following system of linear differential equations:

$$\frac{\mathrm{d}\mathbf{X}}{\mathrm{d}\tau} = \mathrm{A} \cdot \mathbf{X}, \tag{3}$$

where $\mathbf{X}$ is a vector of the isotopic abundances, $\mathbf{X} = (X_{\mathrm{Fe56}}, X_{\mathrm{Fe57}}, \ldots, X_{\mathrm{Ru101}})$, τ is the neutron exposure, and A is the matrix of Maxwellian averaged neutron capture cross-sections and branching ratios for beta decay, with components $\mathrm{A}_{\mathrm{ij}} = -\sigma_i$ for $j = i$, with $\mathrm{A}_{\mathrm{i,j-1}} = +\sigma_i$, $\mathrm{A}_{\mathrm{i+1,j}} = \sigma_i \beta_i$, and $\mathrm{A}_{\mathrm{i+2,j}} = \sigma_{\mathrm{i}}(1 - \beta_i)$, where β_i is the beta decay branching ratio for isotope i at branching points (where applicable). Note $(1 - \beta_i)$ is the β^+ branching ratio, and all other elements in the sparse matrix are zero.

In solving this system, we did not assume a continuous neutron exposure distribution. Instead, different values for single exposures were used. A linear combination of the yields from different single neutron exposures was determined that best fits the abundances of the s-only isotopes in the weak s-process range. In addition, to ensure that the sum of s-only isotopes for the weak and main components were not overproduced with respect to solar,

the abundances to which the *s*-only isotopes were fit were taken as the residuals of the main s-process yields subtracted from the solar abundances. In addition, 15% of the solar ^{80}Kr and 3% of the solar ^{82}Kr were attributed to the νp-process (Käppeler et al. 1989; Pignatari et al. 2010) and likewise subtracted.

We found a linear combination of five neutron exposures that reproduces the desired *s*-only isotopic abundance residuals for ^{70}Ge, ^{80}Kr, and ^{86}Sr Fig. 1. The remaining *s*-only isotopes, ^{76}Se, ^{82}Kr, and ^{87}Sr were under-produced. The only over-productions that resulted were for ^{65}Cu and ^{89}Y. We found the neutron exposures to be: 0.2, 0.25, 0.3, 0.35, and $0.4\,\mathrm{mb}^{-1}$. The respective coefficients that the abundances from each of these exposures were weighted were: 1.5, 0.2, 0.4, 0.6, and 0.7. We attempted to fit as many *s*-only isotopes to their residuals without generating over-productions, and it was not possible to fit all *s*-only isotopes without causing additional isotopic over-abundances. The over-productions of ^{65}Cu and ^{89}Y as well as the under-productions of ^{76}Se, ^{82}Kr, and ^{87}Sr were scaled with the main *s*-process abundances, to fit with the solar abundances. This scaling was equivalent to the scaling done for massive stars and Type Ia yields: the isotopic ratios were preserved.
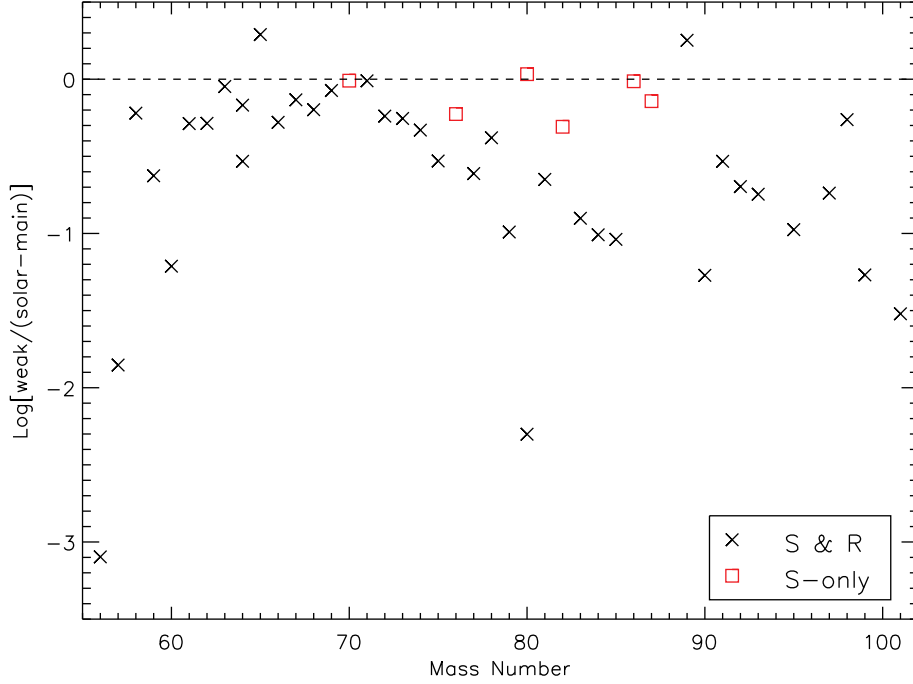
Fig. 1.— The calculated weak s-process contributions to the solar abundance pattern. *Red boxes*: s-only isotopes. *Black x's*: isotopes with contributions from the r- and s-processes. The yields for the s-only isotopes ^{70}Ge, ^{80}Kr, and ^{86}Sr are reproduced well, with underproductions for ^{76}Se, ^{82}Kr, and ^{87}Sr. The only over-productions were for the non s-only isotopes ^{65}Cu and ^{89}Y.

In addition to producing isotopes along the path of stability, there is indication that the weak s-process component in massive stars is responsible for seeding a non-negligible p-isotopic production component. The massive star yields from Rauscher et al. (2002) show significant isotopic productions for ^{74}Se, ^{78}Kr, and ^{84}Sr, which cannot be accounted for by the νp-process (since their stellar models include weak s-process and γ-process reactions, but do not include the νp-process). A mechanism for producing these p-isotopes are γ-process reactions on weak s-process seeds, where the weak s-process would enhance the abundances of unstable proton-rich isotopes which would then undergo photo-disintegration events to give stable p-isotopes. The scaling of these p-isotopic yields should thus track

the weak s-process, rather than the traditional γ-process (as far as its dependence on metallicity), since the abundances are made in-situ from existing weak s-process seeds. It is unclear exactly how much this weak s-process enhanced p-process (WSEP) should contribute to the solar ^{74}Se, ^{78}Kr, and ^{84}Sr abundances. We decided to attribute half of the solar abundances to each the WSEP isotopes and the νp-process for these three p-isotopes.

The uncertainties in our calculation are constrained by the errors of the MACs given in the compilation from the KADoNIS project *www.kadonis.org* (Dillmann et al. 2009), and vary by isotope. We do not propagate the uncertainties through our equations, since our treatment of the weak s-process is only approximate.

2.5.2. Lighter Element Primary Process

Indication for the need of an additional primary process distinct from the r-process appears to be implied by ultra-metal poor (UMP) stellar abundances, and was first implemented by Qian and Wasserburg (2001) in a two component phenomenological model. This process, sometimes referred to as the weak r-process (Truran and Cowan 2000) or charged-particle reaction process (Qian and Wasserburg 2007), was named in more general terms by Travaglio et al. (2004a) as the lighter element primary process (LEPP), and is needed to explain an observed excess of some lower mass ($A < 130$) elements, notably Sr, Y, and Zr, that can not be accounted for by neutron capture processes, photo-disintegration, or CCSNe. Investigation of the triple-α and ^{12}C(α,n)^{16}O rates indicates that their present 2σ uncertainty can not account for the necessary production of Sr, Y, and Zr by the weak s-process in massive stars (Tur et al. 2009). A more recent nucleosynthesis calculation by Arcones and Montes (2011) suggests the interesting possibility of the needed abundances being produced in the neutrino-driven winds of ultra-metal poor (UMP) CCSNe, although their yields suffer over-productions of additional isotopes in order to provide the necessary

Sr, Y, and Zr. In our model we do not separate out the yet unknown LEPP process, but instead the abundances produced by this mechanism are absorbed into the massive star category.

2.5.3. Main S-Process

The main component of the s-process occurs in the thermally pulsating AGB stellar phase for stars with $M \lesssim 1.5 M_\odot$. During hydrogen burning, protons are thought to mix downward into the helium layer, which can then be captured on synthesized ^{12}C to form a ^{13}C pocket (Busso and Gallino 1999). After the subsequent helium flash, α-particles are convectively dredged up through this pocket initiating a neutron source via ^{13}C$(\alpha,n)^{16}$O. This neutron source drives the main s-process by capture on pre-existing metals contained in the star throughout several helium flash cycles. Due to the longer neutron exposures operative in the main s-process (relative to the weak component of the s-process), the main isotopic contributions are isotopes with mass numbers $A \geq 88$ (Iben 1975; Truran and Iben 1977).

The main s-process contributions to the solar abundance pattern were taken from Bisterzo et al. (2011), and these yields were re-normalized to the Lodders et al. (2009) abundances. Many of the s-isotopes with mass numbers $A \geq 88$ were consistent with their solar values, however, some were under-produced. For the under-produced s-only isotopes that fell within 0.1 dex below their solar abundance, we assumed them to be their nominal solar values. This cutoff at 0.1 dex is admittedly somewhat arbitrary. The uncertainties in neutron capture cross-sections and modeling of the AGB stars introduces error, yet remarkably so many s-only isotopes are reproduced by Bisterzo et al. (2011) to within 25% ($\simeq 0.1$ dex) of their solar values. Our choice of this cutoff value acknowledges the existence of errors that are often difficult to enumerate, while assuming that since so many s-only

isotopes are reproduced close to their solar values, the model is likely reliable.

The resulting abundance pattern is given in Fig. 2. Below a mass number of $A = 88$, the s-only isotopes show an explicit drop in their production, and the weak s-process has to contribute in this region to reproduce the needed solar abundances. For mass numbers above $A = 88$, three s-only isotopes are under-produced (by more than 0.1 dex) by Bisterzo et al. (2011): ^{152}Gd, ^{187}Os, and ^{192}Pt. We attributed the residual abundances of these three isotopes to the γ-process. This treatment of the residuals is very approximate, and while ^{152}Gd and ^{192}Pt lie on the proton-rich side of the stability line, ^{187}Os is preceded by the more proton rich ^{184}Os and ^{186}Os, both of which would be more likely candidates for γ-process enrichment. The contribution of ^{152}Gd to elemental Gd is only $\sim 0.2\,\%$, hence relatively little γ-process enrichment is needed to populate the residual abundance. The isotope ^{192}Pt contributes $\sim 0.79\,\%$ to elemental Pt, however, the p-isotope ^{190}Pt contributes even less at $\sim 0.01\,\%$, so it is unlikely that a residual abundance from the γ-process would populate the needed $\sim 0.7\,\%$ ^{192}Pt without also raising the abundance of the more rare ^{190}Pt.
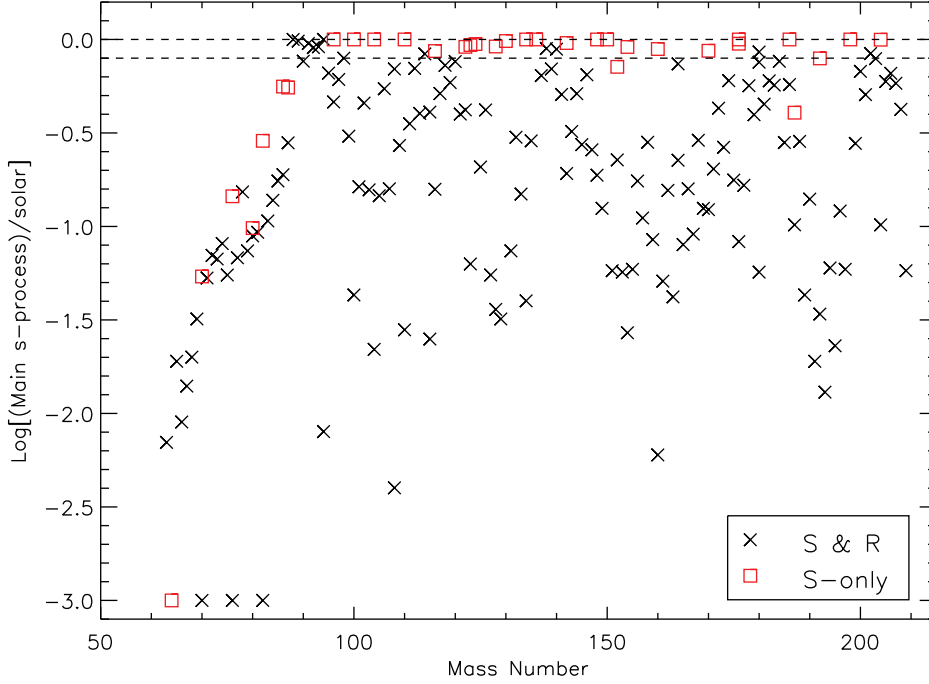
Fig. 2.— Adopted main *s*-process abundances from Bisterzo (2011), relative to the solar abundance pattern. *Red Boxes*: *s*-only isotopes. *Black x's*: isotopes with contributions from the *r*- and *s*-processes. Under-produced *s*-only isotopes that fell within $0.1\,$dex (dashed line) below their solar abundance were assumed to be their nominal solar values.

The main *s*-process produces three characteristic peaks at closed neutron shells, and we sub-divide the main *s*-process abundances into *ls*, *hs*, and "strong" components. The *ls* component is taken to be all abundances from Fig. 3 up to and including Sr, the *hs* component is taken to be all abundances after Sr and up to and including Ba. The strong component is assigned to Pb and Bi isotopes, and is discussed in more detail below. Using the solar main *s*-process abundances given in Fig. 3 as a starting point, we scale the *ls*, *hs*, and "strong" components separately due to the different neutron exposures required for their production.

2.5.4. Strong S-Process

Originally, a strong component of the s-process was introduced to address the underproduction of Pb not accounted for by the main component at solar metallicities (Clayton and Rassbach 1967), and it was believed that a third type of neutron exposure was needed to generate the remaining Pb. Sufficient production was later found to be present in the low metallicity regime of the main component, and the strong s-process component has since been re-interpreted as a low metallicity effect of the main component (Gallino et al. 1998). As the metallicity (and hence Fe) decreases the neutron-to-seed ratio increases, providing a sufficient neutron exposure to make the heavy Pb and Bi isotopes. Simulations of low metallicity AGB stars show production of "strong" s-process isotopes at $[Fe/H] = -2.6$ that exceed production at solar metallicities by several dex, depending on ^{13}C pocket efficiencies (Bisterzo et al. 2010). This implies nearly all of the solar "strong" s-process abundances are made at low metallicities.

Here we continue to refer to Pb and Bi s-process contributions as coming from the "strong" component, since they are scaled distinctly from the hs and ls parts of the main s-process, but it should be noted this is a convention introduced for clarity, and the strong s-process is indeed the low metallicity regime of the main s-process, having a distinctly stronger neutron-to-seed ratio.

2.5.5. R-Process

The r-process synthesizes isotopes beyond the iron peak using rapid neutron capture (relative to the beta decay rate; Burbidge et al. 1957). The location of this process has not been universally accepted, but historically was first thought to occur in CCSNe environments (Hoffman et al. 1997). More recently it has been postulated to occur in shocked surface

layers of O-Mg-Ne proto-neutron stars (Ning et al. 2007; Qian and Wasserburg 2007), and also simulations have shown success in reproducing r-process signatures from ν-driven nucleosynthesis in the He-shell during CCSNe in the low metallicity regime (Z < -3.0; Banerjee et al. 2011). A recent principle component analysis has linked r-process elemental abundances with alpha-elements, further suggesting CCSNe as a possible site for this process (Ting et al. 2012).

The r-process proceeds far beyond the neutron-rich side of stability and (as with the s-process) also bottlenecks at closed neutron shells. Since the closed neutron shells are encountered on the neutron rich side of stability, the proton number is lower at these bottlenecks for the r-process than it is for the s-process, hence after decay to stability the r-process peaks always occur at lower mass numbers relative to the s-process peaks, at approximately 80, 130, and 195. Elements of interest for representing the scaling of r-process elements that have r-only isotopes include germanium, europium, and platinum. The explosive environment of the r-process does not *directly* depend on the initial metallicity of the star, and therefore is primary. Note, however, that the stellar populations that may be responsible for the r-process could depend on Z, e.g., through metallicity-dependence of evolution and stellar mass loss.

The r-process solar abundance contributions were determined using the residual method, in the mass range $69 \leq A \leq 238$. The r-process contributions in the range $56 \leq A \leq 68$ were *not* differentiated from the "massive star category." This choice was made to facilitate the decomposition of the solar abundance pattern in this range, where both CCSNe yields (from α-rich freeze-out, the α-process, and previous nuclear burning) and r-process yields contribute to abundances as primary processes, and are difficult to separate.

2.5.6. P-Isotopes

The νp-process occurs in CCSNe environments where high neutrino fluxes create proton-rich ejecta via weak reactions with neutrons and protons (Fröhlich et al. 2006). Additional neutrino interactions with the left-over protons after α-rich freeze-out produces a neutron abundance, which then undergo (n, p) strong reactions. The resulting protons can then be captured allowing the synthesis of proton rich isotopes up to mass number of $A \simeq 100$ (Fröhlich et al. 2006; Martinez-Pinedo et al. 2006). Since the evolution of this process depends upon ν-interactions with free nucleons, it is independent of the initial star's metallicity, and is considered a primary process.

Proton-rich isotopes beyond mass number $A \simeq 100$ are believed to be created by the γ-process, where successive photo-disintegration events on pre-existing metals occur in the interior layers of supernovae (Woosley and Howard 1978; Rayet and Prantzos 1990). The target nuclei for such events are previously synthesized metals from the r- or s-processes. This process generally begins with (γ, n) reactions moving the target nuclei to the proton rich side of the stability line, where the rate of (γ, p) and (γ, α) start to dominate. Whereas all p-isotope abundances are relatively small and do not dominate their respective elemental abundances, they cannot be accounted for by s- or r-process production, and so both of the p-isotope production processes discussed are required to provide a complete galactic-chemical history.

Similar to the main and weak components of the s-process, we expect to have a transition region between the νp-process and γ-process. A calculation of νp-process yields for a 15M$_\odot$ star was performed by Thielemann et al. (2010). Their results show sufficient production of Mo and Ru isotopes relative to their solar abundances, which is much needed due to well known deficiencies in the γ-process production of these isotopes. From their results, the νp-process yields are shown to decrease quite rapidly beyond mass number

$A = 100$. This suggests that the region of overlap is fairly abrupt, with only ^{102}Pd beyond a peak at ^{98}Ru owing non-negligible fractions of their abundances to the γ-process.

A more complete analysis, perhaps using a grid of stellar masses in order to determine the distribution in the transition region, would likely offer only minor corrections to the final elemental scalings. Instead, new free parameters from the stellar and nucleosynthesis modeling would be introduced. The complete isotopic decomposition for the solar abundance pattern is shown in Section 7.3, and can be used for future isotopic reference.

3. Model Description

Our simple model tries to describe a typical average galactic composition, where the initial state is a homogeneous BBN composition. The final state is taken as a homogeneous composition equivalent to the isotopic solar abundance pattern. Each process responsible for isotopic production (and depletion for the case of D and ^{3}He) is assumed to enrich (deplete) our model galaxy under the instantaneous mixing approximation, to preserve homogeneity across the entire metallicity range considered. Each isotope from our decomposition of the solar abundance pattern is scaled as a function of a chosen normalized dimensionless parameter ξ. At $\xi=0$ the galaxy is in the BBN composition, and at $\xi=1$ the galaxy has the solar composition. The benefit of this choice of parametrization is that its range is congruent with the total metallicity (relative to solar), $Z/Z_{\odot}$. A comparison between ξ and $Z/Z_{\odot}$ is shown in Section 5. This choice of parameter motivates choosing functional forms for the scalings of each process by addressing the predicted dependence on total metallicity these processes would obey. Note that this comparison should not be interpreted as a physical condition imposed upon this parameter. Indeed the parameter ξ is not a physical quantity, rather it is a technical parameter that takes continuous values in the range [0,1], and is chosen to closely approximate Z for ease of discussion. Hence, we assume the relation

between ξ and $Z/Z_\odot$ to be $\log(\xi)=[Z]$. This ansatz is checked later in Section 5.

The parametrization of our model is an attempt to scale the isotopic abundances characterized by typical trends in our Galaxy. For consistency we do not directly use metallicity as the argument of the scaling functions; indeed metallicity is an output of the model, and hence cannot be used as an input. In practice, normalized metallicity $Z/Z_\odot$ tracks ξ very closely, see Fig. 10, and the deviation is typically less than 2%. Whereas our model is not a traditional GCE model that uses scaled stellar yields, our parametrization allows us to improve upon the standard of scaling solar abundances by a constant factor, for use in nucleosynthesis studies.

In the following we address the functional form for each process described in Section 2.

3.1. Massive Stars

The results of massive star simulations for Population III stars (discussed previously in Section 2.4), in addition to being used to compute the solar abundance decomposition, are also used to model the isotopic abundance pattern for $12 \leq A \leq 68$ at a low metallicity of $[\text{Fe/H}] = -3$. The abundances from this simulation were normalized to the ^{56}Fe abundance at $[\text{Fe/H}] = -3$, under assumption that Type Ia contributions to ^{56}Fe are negligible at this metallicity, hence each abundance was multiplied by the factor, $^{56}\text{Fe}_\odot/X_i^{\text{sim}}$, where X_i^{sim} is the abundance of isotope i from the PopIII simulation. These normalized abundances represent a third fixed point for the massive star isotope abundances (in addition to the solar abundances and BBN abundances). Then the massive abundances were interpolated linearly in log-space between their solar values (found in Section 2.4) and their respective abundances given by the normalized PopIII simulation. That is, for each isotope the abundances were scaled according to,

$$\log\left(X_i^*\left(\xi\right)\right) = m_i\left(\log\left(\xi\right) - \log\left(\xi_{low}\right)\right) + \log\left(X_i^{\mathrm{sim}}\right) \tag{4}$$

where $X_i^*\left(\xi\right)$ is the massive abundance of isotope i as a function of the model parameter, and $\log\left(\xi_{low}\right) = -2.5$ (corresponding to a metallicity of $[\mathrm{Fe/H}] = -3$). The slope is defined as, $m_i \equiv \left(\log\left(X_{i,f}^{\mathrm{massive}}\right) - \log\left(X_i^{\mathrm{sim}}\right)\right) / \left(\log\left(\xi_\odot\right) - \log\left(\xi_{low}\right)\right)$, where $X_{i,f}^{\mathrm{massive}}$ is the massive star contribution to the solar abundance (found in Equation 1), and obviously $\log\left(\xi_\odot\right) = 0$. The interpolation given in Equation 4 is extrapolated in both directions from $[\mathrm{Fe/H}] = -3$ to the BBN abundances (zero for these isotopes) and from $[\mathrm{Fe/H}] = 0$ to super-solar values, which gives massive abundances for these isotopes across the entire metallicity range.

As mentioned above, the parameter ξ takes a value of $\log(\xi) = -2.5$ at $[\mathrm{Fe/H}] = -3$. The reasoning behind this choice is as follows. At solar metallicity massive stars are responsible for roughly $30\,\%$ of the total iron, but nearly $100\,\%$ of the alpha isotopes. So then $[\mathrm{Fe}]_{\mathrm{massive}} = -0.5$, and $[\alpha]_{\mathrm{massive}} = 0$. At lowest metallicities, alpha isotopes effectively comprise the aggregate of metals by mass, since secondary sources and Type Ia SNe do not provide enrichment until later. Hence $[Z] \simeq [\alpha]_{\mathrm{massive}}$ holds in low metallicity regimes and will trail $[\mathrm{Fe/H}]$ by a nearly constant $0.5\,\mathrm{dex}$ until Type Ia onset. We then use our model parameter ξ in place of $Z/Z_\odot$. This comparison between ξ and $[\mathrm{Fe/H}]$ is approximate, and relies on the normalized metallicity $Z/Z_\odot$ tracking ξ very closely, see Fig. 10.

3.2. Type Ia SNe

There are three constraints for choosing a parametrization for Type Ia isotopes as a function of ξ. First, Type Ia contributions experience a delay before they begin to enrich the ISM. This is due to the time necessary for, in the accreting white dwarf model, an intermediate to low mass star to evolve through its main sequences and then accrete sufficient material to surpass the Chandrasekhar mass limit. In the meanwhile, massive

stars continue to enrich the ISM, making the galaxy more metal rich. The metallicity at which Type Ia are able to begin contributing to ISM enrichment is typically constrained to the interval $-2 < [\mathrm{Fe/H}] < -1$ depending on environment, galaxy size, etc., but is usually favored towards the upper bound. Hence, Type Ia contributions should be negligible below some value of ξ. Second, upon crossing the Type Ia onset value, contributions should gradually rise to their solar values. Third, at high ξ the scalings should behave essentially like a primary process. Note that this last constraint is an assumption of our model and could be true only for a flat star formation rate (SFR). In fact investigation into Type Ia progenitors by Mannucci et al. (2006) predicts that the ratio of CCSNe to Type Ia rates to be increasing with redshift, a conclusion reached by posing a two component delay time distribution (DTD) progenitor model. If indeed there exists a Type Ia progenitor that operates at low redshifts and experiences a longer delay between the formation of the WD and the later Type Ia explosion (named 'tardy' by Mannucci et al. 2006), a larger number of CCSNe relative to number of CCSNe at the birth of the WD contaminate the ISM, thus increasing the metallicity at a faster rate than it was increasing at the birth of the WD. Hence once the Type Ia SNe do explode, their products would have a metallicity dependence different than linear, due to this increasing rate ratio of CCSNe/SNe Type Ia. We are careful to note that it is unclear exactly how a non flat SFR would impact our scaling for Type Ia SNe, since the above discussion relies on time, and a relation between our model parameter and time cannot be formed. We simply note that there may indeed be an effect. The analogy presented above with respect to flat SFRs serves to construct a rough behavior of Type Ia abundances, and does not mean to attach the physical quantity of time to our model parameter. Furthermore, Type Ia onset may not occur at one unique metallicity, there may be a spread - in how far the different environments have evolved in terms of Z (and O as its main tracer) - when Type Ia sets in. Hence, the corresponding parameter value ξ for Ia onset is not unique for all constituents, but rather just a typical

average that fits the different environments that we sample as as function of it.

One specific form which satisfies all three constraints discussed is given, e.g., by a scaled and shifted hyperbolic tangent base function,

$$X_i^{\text{Ia}}(\xi) = X_{i,\odot}^{\text{Ia}} \cdot \xi \cdot [\tanh(a \cdot \xi - b) + \tanh(b)]/[\tanh(a - b) + \tanh(b)]. \tag{5}$$

The specific value for Type Ia onset is determined by fitting the free parameters, a and b, against available data. Note the hyperbolic tangent function is tempered with a linear factor of ξ to ensure the behavior is linear near solar, where otherwise the $\tanh(x)$ function would asymptote. Note further that whereas this function is phenomenologically motivated it is not unique. The $\arctan(x)$ and $\text{erf}(x)$ also satisfy the above constraints, however, the $\text{erf}(x)$ is more computationally expensive than the $\arctan(x)$ and $\tanh(x)$ functions.

3.3. Neutron Capture and P-Isotopes

The main s-process (ls, hs, and "strong" component), weak s-process, r-process, νp-process, and γ-process contributions are parametrized as power laws,

$$X_i^{\text{strong}}(\xi) = c \left[1 - \frac{\tanh(d \cdot \xi + g)}{\tanh(d + g)} \right] + X_{i,\odot}^{\text{strong}} \tag{6}$$

$$X_i^{\text{ls}}(\xi) = X_{i,\odot}^{\text{ls}} \cdot \xi^l \tag{7}$$

$$X_i^{\text{hs}}(\xi) = X_{i,\odot}^{\text{hs}} \cdot \xi^h \tag{8}$$

$$X_i^{\text{ws}}(\xi) = X_{i,\odot}^{\text{ws}} \cdot \xi^w \tag{9}$$

$$X_i^{\mathrm{r}}(\xi) = X_{i,\odot}^{\mathrm{r}} \cdot \xi^p \tag{10}$$

$$X_i^{\nu\mathrm{p}}(\xi) = X_{i,\odot}^{\nu\mathrm{p}} \cdot \xi^p \tag{11}$$

$$X_i^{\gamma}(\xi) = X_{i,\odot}^{\gamma} \cdot \xi^{\frac{h+p}{2}+1} \tag{12}$$

The free parameters p and h denotes the power of the ξ-dependence for primary and secondary (hs) processes, respectively. The weak component of the s-process was given its own parameter w. The motivation for choosing a power law dependence on these parameters lies in the relations between abundance and metallicity for primary and secondary events, namely that primary events produce abundances linear in metallicity, and secondary produce abundances quadratic in metallicity. The chosen model parameter ξ takes the place of total metallicity (as discussed in the beginning of this Section), and the exponents are parametrized for fitting with data. The metallicity dependence for the γ-process is less clear. It is possible for the target nuclei for this process to be either secondary or primary in origin, and produced in a previous astrophysical environment via the s- or r-process. Hence photo-disintegration events can potentially be a tertiary process. All γ-process isotopes have low ($<$1-10 %) contributions to their respective elemental abundances, hence we chose not to assign a separate free parameter for this process, since the fit to data would likely be poorly constrained. Instead a compromise was struck between the possible s- or r-process origins and the chosen exponent for the γ-process represents an equal primary and secondary seed; about half the metals which might be target nuclei for this process are created by the s-process, and the other half from the r-process. Note that the proposed γ-process abundances enhanced from weak s-process seeds in the WSEP process (discussed at the end of section 2.4.) are scaled the same as the weak s-process, not as γ-process yields.

The choice for the "strong" s-process function is motivated phenomenologically. At low ([Fe/H] $\lesssim -2.0$) metallicities essentially all of the solar abundances for the "strong" s-process have been made. Hence the abundances should be close to constant between $-2.0 \lesssim$ [Fe/H] $\lesssim 0$. Additionally, since AGB stars experience a time delay in their contributions, below [Fe/H] $\lesssim -2.0$ the abundances drop smoothly, hitting zero at some unknown metallicity. The free parameters c, d, and g are used to adjust the shape of the hyperbolic tangent function, and constrain the peak abundance achieved at low metallicity, the metallicity at which the abundances begin to drop to zero, and the rate at which the abundances drop to zero.

3.4. Hydrogen Burning, Classical Novae, ν-Process, and Galactic Cosmic Ray Spallation

The scaling of standard GCR spallation abundances has the same functional form as the s-process scaling. Novae, primary GCR spallation, νp-process, deuterium, and helium (from hydrogen burning) abundances were scaled the same as the r-process, but with an offset added to reflect BBN abundances at $\xi = 0$. The remaining isotope of hydrogen,^{1}H, was scaled according to,

$$X_i^{\mathrm{H}}(\xi) = X_{i,\odot}^{\mathrm{H}} \cdot [1.0 - \xi \cdot Z_\odot - Y(\xi) - D(\xi)], \tag{13}$$

where $Y(\xi)$ is the mass fraction of the helium isotopes, $D(\xi)$ is the mass fraction of deuterium, and $Z_\odot$ is the solar value of total metallicity, given as $Z_\odot$=0.0153 (Lodders et al. 2009). Effectively, this scaling is simply a restatement of the sum of mass fractions, $X + Y + Z = 1$.

4.   Fitting Scaling Model to Observational Data

The isotopic scaling functions were summed into elemental scaling functions for the purpose of fitting the free parameters. An example of this algorithm is given in the Section 7.4. Two compilations of stellar abundance data were used for the fitting. The Frebel (2010) low metallicity data set contains over 1000 stars from the Milky Way (MW) halo and dwarf galaxies. Note that this set is a compilation from various sources and there is hence an unknown source of varying systematic errors. Nevertheless, the spread of the averages of this data (described below) is much bigger than the provided errors and likely spans these systematic errors, though may be subject to systematic offsets. The dwarf galaxy abundances were removed from the set, since it is likely that dwarf galaxies exhibit a different GCE than the MW. In fact a future extension of the current model could be applied to dwarf galaxies to give insight into their GCE relative to the MW. Additionally, Frebel (2010) data from stars in binary systems was removed from the [Ba/Fe] and [Sr/Fe] data, since binary systems experience more enriched s-process abundances due to accretion. Binary stars were identified from the online CHARA catalog http://www.chara.gsu.edu/~taylor/catalogpub/catalogpub.html (Taylor et al. 2003), and were removed from the data set. In addition to removing the known binaries identified by the CHARA catalog, stars that simultaneously satisfied the following criteria: $[Fe/H] < -2.0$, $[Eu/Fe] > 0.5$, and $[Ba/Fe] > 0.0$ were also removed, since they are likely also candidates for binary systems not covered by the CHARA catalog. The other compilation used was the Soubiran and Girard (2005) data set, which contains, in part, 725 stars with magnesium abundances. The Soubiran and Girard (2005) data is needed for high metallicity abundances which fill a paucity of Mg data in the range $-1 < [Fe/H] < 0$ offered by Frebel (2010).

All data is given in units of [X/Fe] as a function of [Fe/H]. The [Fe/H] axis was split into 300 bins in the range $-5 < [Fe/H] < 1$, and the [X/Fe] axis was split into 1500 bins in

the range of the elemental data. Each data point was then assigned a Gaussian distribution using nominal values for the errors in the observations,

$$f_i = \exp\left\{-0.5 \cdot \left([(x_i - x_0)/\sigma_x]^2 + [(y_i - y_0)/\sigma_y]^2\right)\right\}, \tag{14}$$

where f_i is the value of the distribution at bin x_i on the [Fe/H] axis and bin y_i on the [X/Fe] axis, x_0 and y_0 are the [Fe/H] and [X/Fe] values of each data point, and σ_x and σ_y are the nominal errors for each x_0 and y_0. A nominal error of 0.1 dex was assumed for [Fe/H] and [Mg/Fe], and a nominal error of 0.15 dex was assumed for [Ba/Fe], [Sr/Fe], [Eu/Fe], and [O/Fe]. The Gaussian contributions were summed for each bin, and assigned an average and standard deviation for each bin. These binned averages and standard deviations were used for sampling the parameter spaces. We note that all fitting is done in the logarithmic space as is common practice. One could argue that abundances and yields are "additive," hence the linear space should be used. This is left for future work. Indeed fitting in the linear space would be impractical for large dynamic ranges on the one hand; for ratios and small ranges the logarithmic space should suffice.

4.1. Type Ia Parameters

For fitting the Type Ia parameters a, b, and the fraction of the solar ^{56}Fe abundance attributed to Type Ia SNe, f, [Mg/Fe] data was chosen due the large number of data points that exist for this element as well as it owing its abundance to both massive stars and Type Ia SNe. The parameter spaces for a, b, and f were chosen to minimize χ_r^2 between the [Mg/Fe] scaling model and the averages of the binned data. The results are given in Fig. 3.
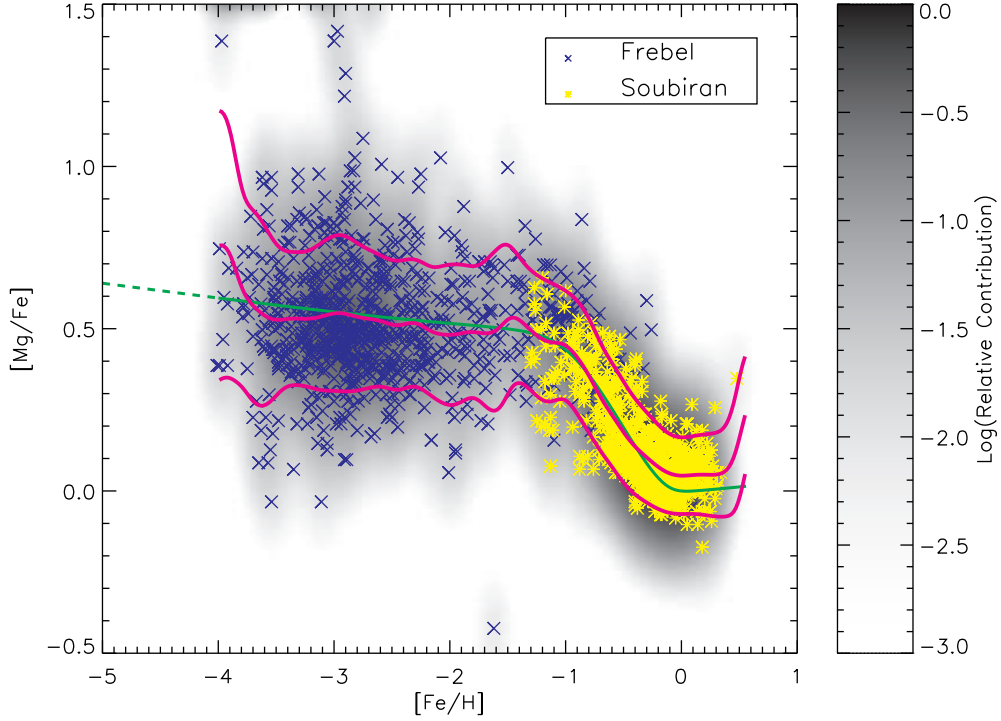
Fig. 3.— The resulting model for [Mg/Fe] found by parameter fitting. *Blue x's*: Frebel (2010) data points. *Yellow asteriks*: Soubiran and Girard (2005) data. The dark shadow background shows the errors in the data, depicted by a Gaussian distribution about the data points. The averages and standard deviations for the Gaussian contributions per bin are given by the central and exterior solid thick (pink) lines, and the model itself is shown as a solid thin (green) line. There are a couple outlying data points on the graph whose Gaussian contributions can be seen at the upper limit of the [Mg/Fe] axis.

As shown in Fig. 3, the magnesium scaling falls well within the standard deviation of the data, and tracks the average well. The determined best fit parameter values are $a = 5.024$, $b = 2.722$, and $f = 0.693$, with a resulting $\chi^2_r = 0.0317$. This low χ^2_r reflects the large spread inherent in stellar abundances and the observational uncertainties that exist, and also the fact that the bins (and data) are not uncorrelated, as each star is "spread" out over many bins due to the assigned Gaussians. The drop of the curve to solar values

from its peak at [Fe/H] $\simeq -1$ is caused by Type Ia onset, when Fe production begins to dominate over magnesium.

The relatively flat line (only ≈ 0.1 dex drop in [Mg/Fe] over 2 dex in [Fe/H]) depicted in the figure below [Fe/H] $\lesssim -4$ describes magnesium and iron abundances scaling together. This is a consequence of our model assuming massive stars are the sole and unique source of metals at low metallicity. Whereas it is likely that magnesium and iron co-evolve in this range, due to their shared primary (massive star) origin that dominates at low metallicities, it is unsubstantiated from any data that the correlation is as exact as the model forces it to be. Indeed, the model cannot predict abundances below [Fe/H] $\simeq -4$ with any reliability, given the paucity of data at such low metallicities. It could be argued that "average" scaling of abundances is not even a well defined concept in this range, since individual astrophysical events can have such a large stochastic effect on the metallicity content. In this sense, our model assumes "scaling" is a consequence of varying amounts of mixing with BBN from the same stellar sources, and until sufficient stellar events can reliably produce an average, our model is not a statistically accurate description of this mixing.

4.2. R-Process and *hs* Parameters

For determining the value for the r-process parameter p, the chosen data was [Eu/Fe]. Europium is an r-process peak element with two isotopes, ^{151}Eu and ^{153}Eu, both of which have dominant ($\sim 85\,\%$ its solar value) contributions from the r-process. We determined the optimized value for p using data from the Frebel set (2010). The best fitting scaling for [Eu/Fe] is given in Fig. 4.
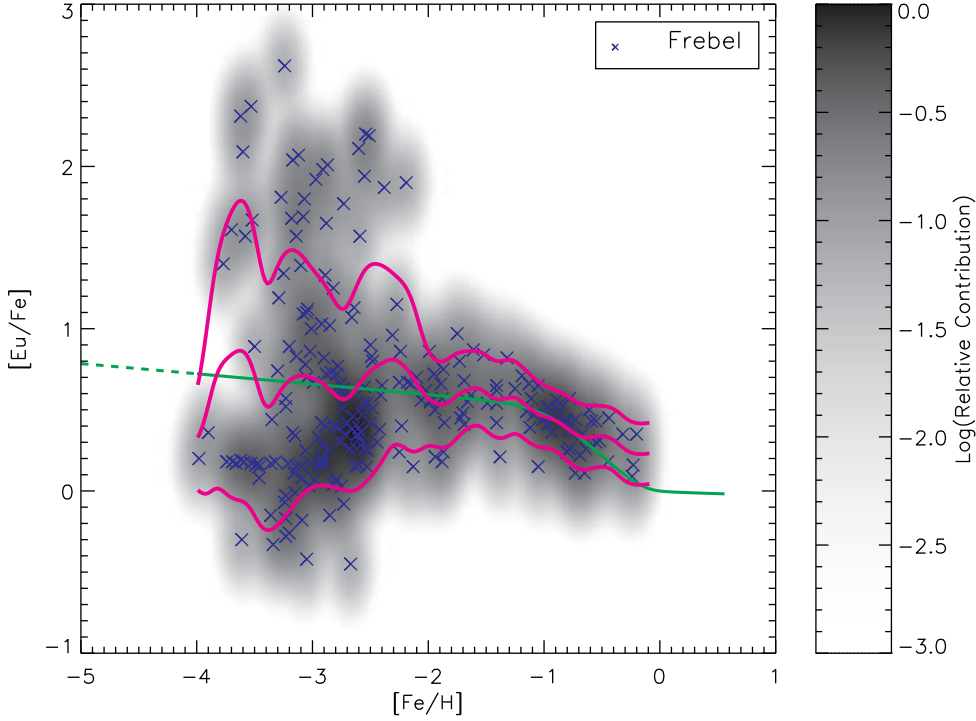
Fig. 4.— The resulting model for [Eu/Fe] found by parameter fitting. The full scaling is shown in the thin solid (green) line. *Blue x's*: Frebel (2010) data points. The rest of the figure follows the convention of Fig. 3.

The best fit parameter value was found to be $p = 0.938$ with $\chi_r^2 = 0.040$. The previously found best fit values for a, b, and f (from Section 4.1) were used for Fe. Note that a nominal value of $h = 1.5$ for the s-process parameter was assigned for the purpose of fitting the [Eu/Fe] model. The choice of this nominal value for h has a negligible impact on the best fit value for p due to the small s-process component of Eu, and for comparison an optimization of the parameter space for p with an h value of 2 yields a best fit value of $p = 0.935$ with $\chi_r^2 = 0.041$, a difference of 0.3 % in p, and a difference of 2.5 % in χ_r^2.

For fitting the values for the heavy main s-process parameter h, the chosen data was [Ba/Fe]. This element has two s-only isotopes, ^{134}Ba and ^{136}Ba, along with three isotopes with contributions from both the s- and r-processes, ^{135}Ba, ^{137}Ba, and ^{138}Ba, and a small

elemental contribution ($\sim 0.2\%$ its solar value) from two γ-process isotopes, ^{130}Ba, and ^{133}Ba. In Fig. 5, we plot results for the scaling of barium with the best fit value for h. The previously found best fit values (from Section 4.1) for a, b, f, and p were used for Fe and the r-process contributions to Ba.
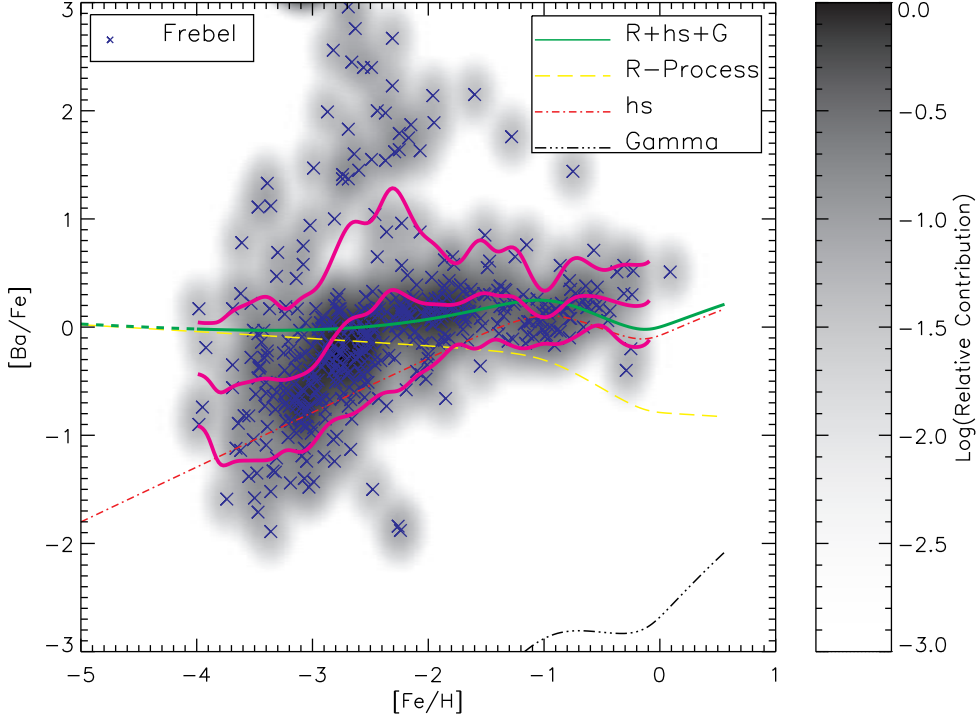
Fig. 5.— The resulting model for [Ba/Fe] found by parameter fitting. The full scaling is shown in the solid thin (green) line, with the heavy s-process, r-process, and γ-process components plotted in dot-dashed (red), long-dashed (yellow), and dot-dot-dot-dashed (black) lines, respectively. *Blue x's*: Frebel (2010) data points. The rest of the figure follows the convention of Fig. 3.

The minimized value of $\chi^2_r = 0.134$ was obtained from the parameter value $h = 1.509$. The trend of our barium model at low ($\lesssim -2.0$) metallicities implies abundances that begins to track iron. At these low metallicities, iron production is dominated by primary massive star contributions, as is barium production dominated by the primary r-process,

hence the [Ba/Fe] encounters a "floor" in its abundances, as is expected (e.g., Truran 1981).

Above [Fe/H] $= -1.793$, secondary contributions from the s-process exceed r-process contributions, and begin to drive [Ba/Fe] upward to a local maximum, before Type Ia contributions take the ratio back down to solar. This metallicity value of [Fe/H] $= -1.793$ where heavy s-process contributions equal r-process contributions is lower than the typical value of [Fe/H] ≈ -1.5 (found by, e.g., Travaglio et al. 1999; Truran 1981), and is due to our main heavy s-process exponent being smaller than the theoretical value of 2. Note that at all metallicities, the γ-process contributions to elemental abundances are negligible.

4.3. Weak S-Process and ls Parameter

The parameters constraining the weak s-process and ls scalings are w and l. Ideally one would wish to use [Ga/Fe] or [Se/Fe] elemental data, both of which have significant weak s-process isotopic contributions to their elemental abundances (≈ 0.61 for Ga, ≈ 0.21 for Se), as well as also lying on the first main s-process peak. Unfortunately data across a sufficient metallicity range for these elements is sparse, and [Sr/Fe] data is used instead, which has ≈ 0.09 of its elemental abundance due to the weak s-process. In addition to Frebel (2010) data, two additional sources were used that provide observations of higher metallicity stars (Taylor et al. 2003). Sr has two s-only isotopes along the weak s-process path, ^{86}Sr and ^{87}Sr, along with one mixed isotope of r- and s-process origin, ^{88}Sr (although the r-process component is negligible), and one νp-process isotope, ^{84}Sr. Possible binary contamination of the data was removed according to the same prescription adopted for the [Eu/Fe] data. In Fig. 6 we plot results of the model for strontium with the best fit value for w and l. The previously found best fit values for a, b, f, and h (from Section 4.1 and 4.2) were used for Fe and the main s-process contributions to Sr.
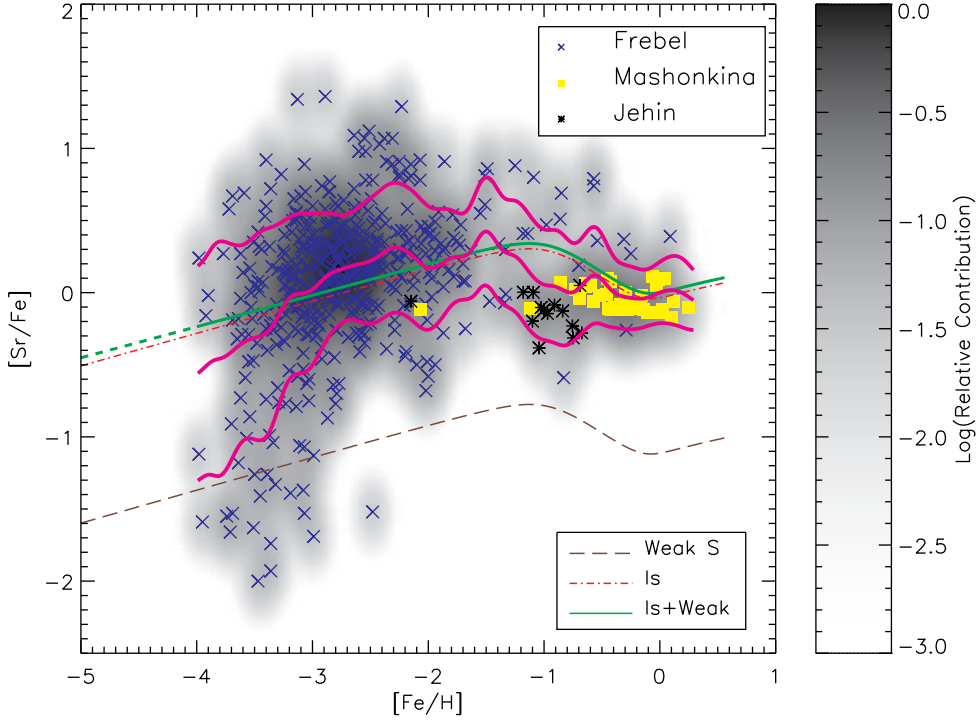
Fig. 6.— The resulting model for [Sr/Fe] found by parameter fitting. The full scaling is shown in the solid thin (green) line, with the light s-process and weak s-process components plotted in dot-dashed (red) and long-dashed (brown) lines, respectively. *Blue x's*: Frebel (2010) data points. *Yellow crosses*: Mashonkina and Gehren (2001) data points. *Black asteriks*: Jehin et al. (1999) data points. The rest of the figure follows the convention of Fig. 3.

The value of $\chi_r^2 = 0.061$ was obtained from the parameter value $w = 1.230$ and $l = 1.227$. At all metallicities, contributions from the light s-process exceed weak s-process contributions, and the νp-process and r-process contributions are negligible.

4.4. "Strong" S-Process Parameter

The final free parameter constrains the third *s*-process peak. Pb data was taken from Frebel (2010), and binary stars were removed. The remaining data set consists of four points only. Due to the paucity of data, our usual standard of optimizing the elemental scaling using a χ_r^2 analysis poorly constrains [Pb/Fe]. Instead, the functional form given in Section 3.3 was used to fit the free parameters c, d, and g by hand to the four data points. The result is given in Fig. 7.
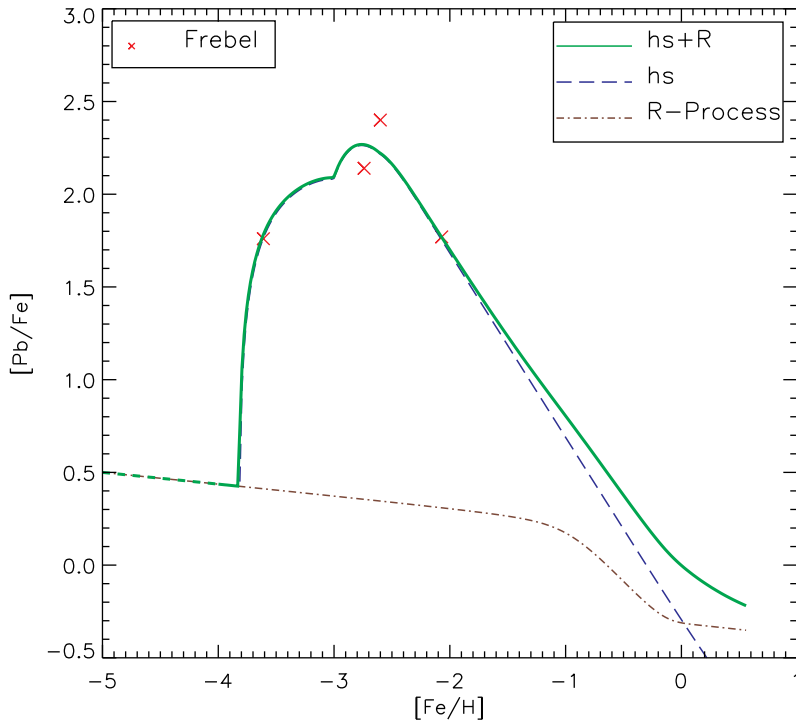
Fig. 7.— The resulting model for [Pb/Fe] found by parameter fitting by hand. The full scaling is shown in the solid thin (green) line, with the heavy *s*-process and r-process components plotted in long-dashed (blue) and dot-dashed (brown) lines, respectively. *Red x's:* Frebel (2010) data points.

As shown in Fig. 7, [Pb/Fe] peaks at [Fe/H] ≈ -2.5, consistent with the AGB simulations by Bisterzo et al. (2010). Below [Fe/H] $= -2.5$, [Pb/Fe] drops until the

"strong" s-process component vanishes, and the elemental scaling is determined only by the r-process. The free parameters were found to be $c = -2 \cdot 10^{-11}$, $d = 200$, and $g = -0.23$. It should be noted that the few data points can only constrain the peak of the [Pb/Fe] fit, and the drop of the abundance at [Fe/H] ≈ -3.6 is not motivated by the data, but is an artifact of our chosen function for "strong" s-process evolution. It is clear that [Pb/Fe] should indeed drop, as AGB stars do not produce isotopes at arbitrary low metallicities, but the exact nature of the drop to the r-process may not be well represented by our model.

Furthermore, the "kink" at [Fe/H] $= -3$ results from the change in slope of the Fe scaling. As discussed in Section 3.1, massive star contributions are linearly interpolated between their solar values and the values at [Fe/H] $= -3$ given by the massive star simulation. Below [Fe/H] $= -3$, massive star contributions are sent linearly to zero (in linear space). This treatment changes the slope of [Fe] on either side of [Fe/H] $= -3$, which manifests as the observed "kink" in Fig. 7. In reality we would expect a broad peak rather than the shown narrower peak following a kink before descent to the r-process floor. This very rough treatment of the "strong" s-process results in larger uncertainties for the s-process contributions to Pb and Bi isotopes from our model at metallicities below [Fe/H] < -2.5, and further revision is left to future work.

5. Results and Discussion

The functional forms for all scalings are now fixed by adjusting model to optimally fitting the observational data. A comparison is given in Fig. 8.
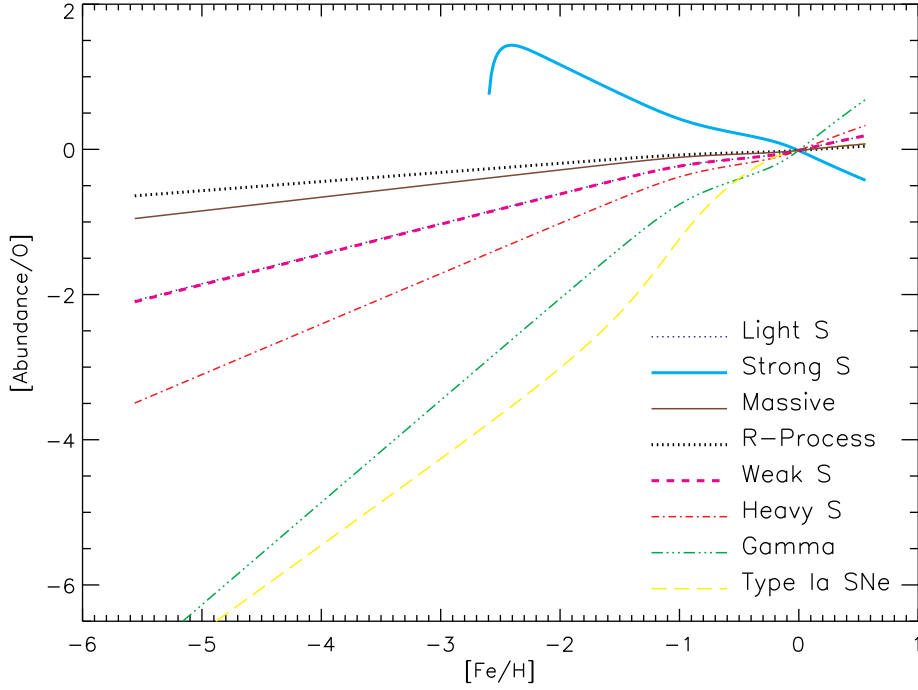
Fig. 8.— The scaling functions of the model contributions relative to oxygen as functions of metallicity. The "Massive" line shows the scaling of the massive category's contribution to ^{56}Fe, and is normalized to the solar contribution from this category only.

Since each isotopic contribution in the "massive" category is independently interpolated between solar and [Fe/H], the "massive" (brown thin solid line) scaling shown in Fig. 8 is an example, and what is shown is the scaling for the massive contribution to ^{56}Fe only. Hence, this scaling gives $[^{56}\text{Fe}_{\text{massive}}/\text{O}] = \log\left(^{56}\text{Fe}_{\text{massive}}/^{56}\text{Fe}_{\text{massive},\odot}\right) - \log\left(\text{O}/\text{O}_\odot\right)$, where $^{56}\text{Fe}_{\text{massive},\odot}$ is the massive contribution to the solar abundance of ^{56}Fe.

Type Ia SNe (yellow long-dashed line) contributions are negligible ($< 1\,\%$ the solar value) below the Type Ia onset identified by our model. After Type Ia onset at [Fe/H] ≈ -1.1, the contributions climb smoothly to solar. It is concerning that the Type Ia scaling begins to flatten at low metallicities until its slope becomes less than the γ-process (green dot-dot-dot-dashed line). Whereas contributions are negligible at these metallicities,

the tanh(x) function chosen for Type Ia fails to describe the accurate physical picture, as the slope ideally should increase sharply below onset to reflect Type Ia "turning on." We accept this behavior for the Type Ia scaling in part because contributions are already negligible and would offer insignificant corrections to the isotopic abundances if changed. Even though our Type Ia scaling has a negligible impact on the abundances below the onset value, its description in this range is not constrained at low metallicities. In the present model it is only important for [Fe/H] > −1.1. Furthermore, the elemental data ends at [Fe/H] ≈ −4, and hence the only constraint on Type Ia scaling below this metallicity (where it flattens out) is that there is no contribution from the BBN composition.

Both the massive star (brown solid line) and r-process (black thick dotted line) scalings show similar trends at all metallicities, due to their shared primary nature. Abundances for the γ-process and νp-process are scaled the same as the heavy s-process and r-process, respectively.

Both components of the s-process do not show the typical behavior of secondaries. The heavy component (red dot-dashed line) shows a higher drop off at lower metallicities than the primary processes, but with a slower exponent of 1.509 compared to the theoretical value of 2. The light s-process (blue dotted line) and weak s-process (thick pink dashed line) scalings behave similarly at all metallicities, with an exponent intermediate between the heavy s-process and primary processes. The "strong" component (light-blue thick solid line) displays supra-primary behavior above [Fe/H] ≈ −2.5, as is expected from its high abundance at low metallicities. Below [Fe/H] ≈ −2.5 it decreases at a rate larger than any other process, until its contributions become zero and the scaling is no longer plotted. In this range [Fe/H] ≲ −2.5 it is unlikely that our model correctly describes the "strong" component, as the scaling here is unconstrained by data.

The failure of our model to reproduce the theoretical secondary nature is not new,

and this discrepancy has been previously observed in the data (Prantzos 2011). It may be possible to alleviate this discrepancy by noting that at low metallicities rotating massive stars may have an increased neutron exposure in two different ways. The first is enhanced nitrogen production from CNO burning, which then burns into neon to seed the neutron source (Pignatari et al. 2008; Frischknecht et al. 2010). The second is an earlier ^{22}Ne ignition due to higher core temperatures (Frischknecht et al. 2010). The effect of this larger neutron exposure is enhanced weak s-process production at low metallicities, driving an increase in the abundance and resulting in a parameter value that is closer to a primary rather than secondary process.

Explaining the discrepancy for the heavy and light components is more challenging. It may be plausible, however, that we are observing the net result of a mixed isotopic history. That is, one could imagine a composition with a given abundance of an isotope made from a primary process in some astrophysical environment, that is then processed in a different astrophysical environment at a later time. If another abundance of this isotope is then made from a secondary process in the new astrophysical environment, its history would change from primary to secondary. Our model offers no way to track this effect. Indeed the aggregate of these effects may be in fact what we observe, and hence may be why our model gives an averaged main component parameter that deviates from the theoretical value of 2.0. Of course, this only applies to elements whose isotopic contributions can be made from both primary and secondary sources. In Section 7.2 we summarize our optimized parameter values. The complete scaling model for all elements is shown in Fig. 9.
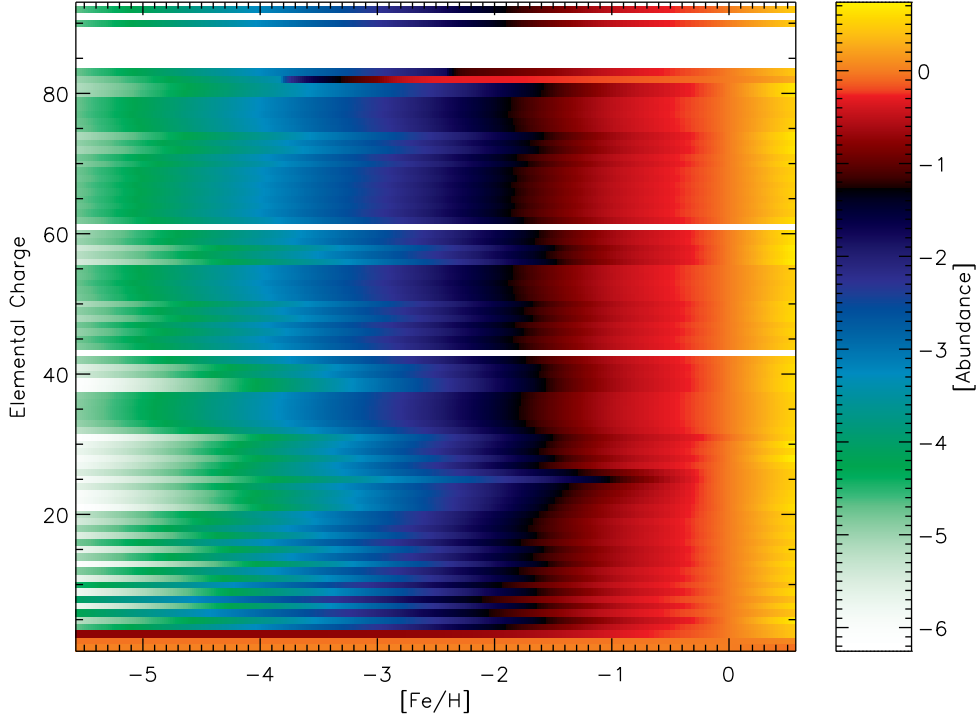
Fig. 9.— The complete elemental scaling of the model. The abundances are given relative to their solar values.

The traditional method of scaling solar abundances for inputs into stellar simulations is equivalent to treating the Galaxy as though all isotopic production is primary. A plot representing this approximation would be similar to Fig. 9, but with all metals changing their relative abundances at the same [Fe/H], which would look like a type of "flag" pattern, with all colors (representing relative abundances) changing together. In contrast to this approximation, Fig. 9 shows the corrections offered by our model to the traditional approximation due to the inclusion of Type Ia onset and secondary processes. These corrections are identifiable as "fingers" which protrude in the horizontal axis, distorting the otherwise clean "flag" pattern, and occurring at elements that either lie on the Fe-peak or that have strong secondary or other Type Ia contributions.

The scalings that notably stand apart from the others are the light elements: H, He,

and Li. These begin with a much higher relative abundance (compared to the metals) due to BBN, and so change less, relative to their solar values compared to the other elements that begin with zero BBN contributions. Additionally, Pb displays a relative higher abundance at low metallicities due to the "strong" s-process. The sharp drop of Pb at $[\mathrm{Fe/H}] \approx -3.8$ is consistent with Fig. 7, and is a very approximate treatment.

In Section 7.4, we give the ratios of the isotopic abundances from our scaling model over the abundances generated from a linear interpolation between BBN and solar. The ratios are computed for two sub-solar metallicities ($[Z] = -1$ and $[Z] = -3$), and illustrate the corrections the model provides to the standard approach.

Finally, our choice for the model parameter ξ can now be compared to the normalized metallicity $\mathrm{Z/Z_\odot}$. The plot is given in Fig. 10.
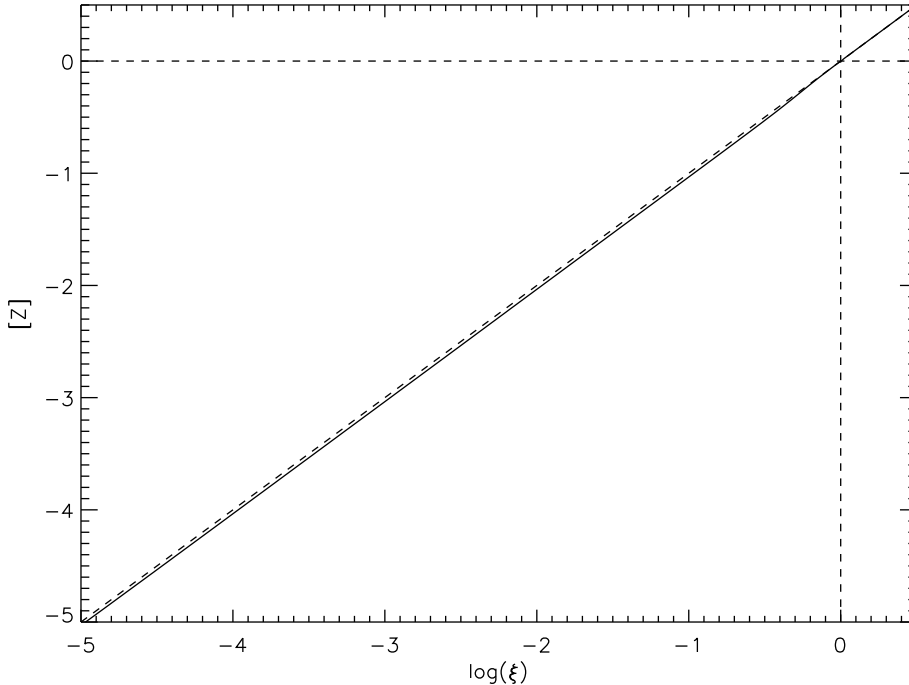
Fig. 10.— Comparison of our model parameter with $\mathrm{Z/Z_\odot}$. The behavior is linear to within 2% for all values of $\log(\xi)$ and $\mathrm{Z/Z_\odot}$. The dashed lines demarcate the origin, and display

the unity line for comparison.

As shown in Fig. 10, our choice for the model parameter indeed corresponds to $Z/Z_\odot$ to within 2% for all values. The deviation from true linear occurs close to solar metallicity, when Type Ia SNe contributions become important and produce a small, almost unidentifiable "bump" near $[Z] \approx -0.2$. This comparison verifies our motivation for choosing functions for primary and secondary processes as being proportional to a polynomial of ξ.

6. Conclusions

A metallicity-dependent Galactic isotopic decomposition for all stable isotopes has been constructed. The solar abundance pattern was decomposed into several astrophysical processes responsible for isotope synthesis. Parametric functions were chosen to scale the contributions from each astrophysical process to give isotopic abundances, with the solar abundance pattern and BBN used as boundary conditions. The isotopic scalings were summed into elemental scalings and compared with stellar data in the halo and disk to tune the fit parameters of the model. The final scalings provide a complete isotopic abundance pattern at any desired metallicity. The purpose of this work is to provide *isotopic* abundances that can be used as initial abundances for stellar models in future work, or other nucleosynthesis studies. Our model is a large improvement over approximating the input *isotopic* abundance pattern by simply scaling the solar abundances, and/or using solar isotopic ratios. This is the first time this has been done in a systematic way.

The interpretation of our offered solar abundance pattern decomposition is approximate, as different assumptions (of varying reliability) operate for different isotopes. The decompositions of the light isotopes (below carbon) likely reflect the best current understanding, however, the current understanding is admittedly an area of ongoing

investigation. The decomposition from carbon up to the Fe peak from massive stars and Type Ia SNe are the result of scalings done on data from two models that preserve the isotopic ratios across the two models, which distorts the original abundance patterns taken from the simulations. Whereas this preserves the salient features of these two processes, it should be noted that the isotopes that are not CNO or Fe peak suffer a larger uncertainty in their decompositions due to this scaling. Furthermore we make no distinction between the several operative primary processes that fall under the category of "massive stars," which are dominated by CCSNe yields but also necessarily include yields from stellar winds of lower mass stars, ν-process, and classical novae.

The main s-process yields used show good agreement with the solar abundances, however, the weak s-process computation only reproduces the necessary abundances for three of the six s-only isotopes along the weak s-process path. The method for computing the weak s-process should ideally rely upon stellar models, unfortunately the results often display over-productions of several isotopes above their solar values. Our more simple approach, whereas less robust, has the advantage of only two isotopic over-productions, and is calculated directly from the neutron capture cross-sections and branching ratios.

In addition to providing isotopic abundances for input into stellar simulations, our methodology can also be applied to model other systems such as dwarf galaxies, and tailoring the free parameters to relevant data sets will then yield approximate chemical abundances for such systems. Yet another application lies with stellar model fits. Currently published stellar evolution models only give average yields for stars over certain mass ranges. These averages must be fitted to available observational data sets, as done for example by Heger and Woosley (2010). The need for this fit is evident, since stellar models only address the stellar nucleosynthesis part of GCE and neglect several processes which will ultimately influence the subsequent ISM abundances over many stellar lifetimes, processes

such as infall and ISM mixing. The age of the Galaxy (or timescale of GCE) is much greater than the typical stellar lifetimes that contribute significantly to ISM enrichment; hence this fitting is required to give stellar yields a more precise physical meaning in a GCE context. Thus in addition to providing the initial isotopic abundances for input into stellar simulations, the abundances can also be used to fit the resulting stellar yields from the model in a consistent fashion.

This work has laid out a basic method of isotopic decomposition as a function of metallicity based on elemental observational data and underlying nucleosynthesis processes for a complicated environment like the Galaxy. Future work should have a more detailed look at specific and less complicated environments like, e.g., dwarf galaxies that have different contributions and would hence allow one to constrain model parameters more uniquely (such as Type Ia onset contributions). Another challenge will be to relate and identify the different nucleosynthesis processes with the principle components found in observational work like that of Ting et al. (2012), and help to improve such principle component analysis based on physical nucleosynthesis processes.

7. Appendix

7.1. Fitting Procedure

Here we explain the general algorithm for constructing elemental ratios [X/Fe] from the isotopic scaling functions, and fitting to data. A specific example will then be given.

A) For each isotope i of element X, write the scaling function, $X_i(\xi)$, for all processes that contribute to the solar abundance of X_i, using Equations 4-13 and the solar abundance decomposition in Section 7.3. This gives a scaling relation for the isotope as a function of ξ, with one or more free parameters.

B) Sum the isotopic scaling relations to give an elemental scaling relation,

$$X(\xi) = \sum_i^n X_i(\xi), \tag{15}$$

where n is the number of isotopes that comprise element X.

C) Repeat this process for the elements Fe and H.

D) The ratios [X/Fe] and [Fe/H] can then be evaluated, which are functions of ξ and one or more free parameters. For specific free parameter values, a curve can be plotted in the [X/Fe] and [Fe/H] plane.

E) Observational data is then plotted on this plane, and each data point is assigned a gaussian spread (Equation 14), and the gaussian contributions in x- and y-axes are binned and averaged (Section 4).

F) A χ_r^2 analysis is performed for the free parameter values in [X/Fe] and [Fe/H]: for each free parameter value a curve is defined for [X/Fe] vs. [Fe/H], and the best-fit parameter value is chosen that minimizes the χ_r^2 between the curve and the averaged data.

This defines a unique curve for [X/Fe] vs. [Fe/H], and hence also gives unique functions for the elemental *and isotopic* scaling functions.

We now give a specific example of the above steps A - C, for making the elemental ratios [Au/Fe] and [Fe/H]. Note the above steps D - F comprise Section 4 for the elements Mg, Eu, Ba, Sr, and Pb.

We first consider Au, which has only one stable isotope. The solar abundance for ^{197}Au has *hs*-process and *r*-process components (Section 7.3), hence these abundances scale as follows (using Equations 4-13):

$$^{197}\mathrm{Au}(\xi) = {}^{197}\mathrm{Au}^{\mathrm{s}}_{\odot} \cdot (\xi)^h + {}^{197}\mathrm{Au}^{\mathrm{r}}_{\odot} \cdot (\xi)^p, \tag{16}$$

where $^{197}\mathrm{Au}^{\mathrm{s}}_{\odot}$ is the portion of the solar abundance of ^{197}Au from the *hs*-process (according to our solar abundance decomposition, see Section 7.3). Similarly, $^{197}\mathrm{Au}^{\mathrm{r}}_{\odot}$ is the portion of the solar abundance of ^{197}Au from the *r*-process. For illustration, we can evaluate $^{197}\mathrm{Au}(\xi)$ at $\xi = 0, 1$:

$$^{197}\mathrm{Au}(\xi = 0) = 0, \tag{17}$$

$$^{197}\mathrm{Au}(\xi = 1) = {}^{197}\mathrm{Au}^{\mathrm{s}}_{\odot} + {}^{197}\mathrm{Au}^{\mathrm{r}}_{\odot} = {}^{197}\mathrm{Au}_{\odot}. \tag{18}$$

Observe that Equation 17 gives the BBN abundance of ^{197}Au, whereas Equation 18 gives the solar abundance. When ξ takes a value in between 0 and 1, we get a ^{197}Au abundance that is in between BBN and solar. This holds for all elemental scalings (all scaling functions are monotonic). We now have a scaling relation for ^{197}Au using the continuous technical parameter ξ. Note the function $^{197}\mathrm{Au}(Z/Z_{\odot})$ also must go from BBN to solar for

$Z/Z_{\odot} \in [0, 1]$. Since Au is a mono-isotopic element, the function of its isotope is also the function of its element, $^{197}\mathrm{Au}(\xi) = \mathrm{Au}(\xi)$.

The 4 stable isotopes of Fe have massive, Type Ia, and weak s-process contributions (using Equations 4-13),

$$^{54}\mathrm{Fe}(\xi) =^{54} \mathrm{Fe}_{\odot}^{\mathrm{Ia}} \cdot \xi \cdot [\tanh(a \cdot \xi - b) + \tanh(b)] / [\tanh(a - b) + \tanh(b)] +^{54}\mathrm{Fe}_{\odot}^{*} \cdot 10^{m_{Fe54} \cdot (\log(\xi) - \log(\xi_{low})) + \log(X_i^{\mathrm{sim}})},$$
(19)

$$^{56}\mathrm{Fe}(\xi) =^{56} \mathrm{Fe}_{\odot}^{\mathrm{Ia}} \cdot \xi \cdot [\tanh(a \cdot \xi - b) + \tanh(b)] / [\tanh(a - b) + \tanh(b)] + \mathrm{Fe}_{\odot}^{*} \cdot 10^{m_{Fe56} \cdot (\log(\xi) - \log(\xi_{low})) + \log(X_{Fe56}^{\mathrm{sim}})},$$
(20)

$$^{57}\mathrm{Fe}(\xi) =^{57} \mathrm{Fe}_{\odot}^{\mathrm{ws}} \cdot \xi^{w} +^{57} \mathrm{Fe}_{\odot}^{*} \cdot 10^{m_{Fe57} \cdot (\log(\xi) - \log(\xi_{low})) + \log(X_{Fe57}^{\mathrm{sim}})},$$
(21)

$$^{58}\mathrm{Fe}(\xi) =^{58} \mathrm{Fe}_{\odot}^{\mathrm{ws}} \cdot \xi^{w} +^{58} \mathrm{Fe}_{\odot}^{*} \cdot 10^{m_{Fe58} \cdot (\log(\xi) - \log(\xi_{low})) + \log(X_{Fe58}^{\mathrm{sim}})}.$$
(22)

We then find the function for elemental Fe, $\mathrm{Fe}(\xi) =^{54} \mathrm{Fe}(\xi) +^{56} \mathrm{Fe}(\xi) +^{57} \mathrm{Fe}(\xi) +^{58} \mathrm{Fe}(\xi)$. The ratio $[\mathrm{Au/Fe}] = \log(\mathrm{Au}(\xi)/\mathrm{Au}_{\odot}) - \log(\mathrm{Fe}(\xi)/\mathrm{Fe}_{\odot})$ can then be constructed (which is a function of ξ). To find [Fe/H], we consider the scaling functions for deuterium and $^{1}\mathrm{H}$:

$$\mathrm{D}(\xi) = \mathrm{D}_{\odot} \cdot \xi^{p} + \mathrm{D}_{\mathrm{BBN}},$$
(23)

$$^1\mathrm{H}(\xi) = {}^1\mathrm{H}_\odot \cdot [1.0 - \xi \cdot Z_\odot - \mathrm{Y}(\xi) - \mathrm{D}(\xi)], \tag{24}$$

where $\mathrm{D_{BBN}}$ is the BBN abundance of deuterium. The helium function $\mathrm{Y}(\xi)$ is the sum of the isotopic scalings of its two stable isotopes:

$$^3\mathrm{He}(\xi) = {}^3\mathrm{He}_\odot \cdot \xi^p + {}^3\mathrm{He_{BBN}}, \tag{25}$$

$$^4\mathrm{He}(\xi) = {}^4\mathrm{He}_\odot \cdot \xi^p + {}^4\mathrm{He_{BBN}} \tag{26}$$

The elemental function for H is then, $\mathrm{H}(\xi) = {}^1\mathrm{H}(\xi) + \mathrm{D}(\xi)$, and [Fe/H] can be found. The specific values used for the free parameters h, p, a, b, and w are given in Section 7.2. This defines a unique curve in the [Au/Fe] vs. [Fe/H] plane. All free parameter values are determined by fitting the elemental functions [Mg/Fe], [Eu/Fe], [Ba/Fe], [Sr/Fe], and [Pb/Fe] to observational data (Section 4). Using using Equations 4-13, Section 7.3, and Section 7.2 all elemental ratios and isotopic functions can be evaluated.

7.2. Free Parameter Values

Table 1 summarizes the optimized parameter values found by fitting to data.

Table 1.   Optimized Parameter Values

Parameter	Best-fit Value	Description
a	5.024	Type Ia tanh Scaling Factor
b	2.722	Type Ia tanh Shifting Factor
f	0.693	Fraction of Solar ^{56}Fe from Type Ia
p	0.938	Primary Process Exponent
h	1.509	hs-process Exponent
l	1.227	ls-process Exponent
w	1.230	Weak s-process Exponent
c	-2.e-11	"Strong" tanh Coefficient
d	200	"Strong" tanh Scaling Factor
g	-0.23	"Strong" tanh Shift Factor

7.3.   Solar Abundance Decomposition

Table 2 shows the solar abundance pattern decomposition for all stable isotopes into the various astrophysical processes employed by the model: Big Bang Nucleosynthesis, ν-process/primary galactic cosmic ray spallation/novae yields (together in a single category), secondary galactic cosmic ray spallation, massive star yields (includes CCSNe, stellar winds, ν-process, and r-process contributions from carbon through zinc), Type Ia SNe yields, main s-process (which include all of "strong", ls, and hs components), weak s-process, νp-process, γ-process, and the r-process (from zinc through uranium). The solar abundances in column 2 are from Lodders et al. (2009) and are in units of mole fractions. The various astrophysical processes in columns 3-12 show the fraction of the solar abundance attributed to each process, and these fractions can be used to decompose any desired solar abundance pattern. The fraction values are rounded to three significant figures. Note that the remaining helium not made in BBN is from hydrogen burning, which not explicitly shown in the the table.

Table 2. Solar Abundance Decomposition

Ion	Solar	Main S	Weak S	R	νP	γ	Ia	Massive	GCR	ν/Novae/GCR	BBN
H1	7.0571E-01	⋯	⋯	⋯	⋯	⋯	⋯	⋯	⋯	⋯	1.06
H2	1.3691E-05	⋯	⋯	⋯	⋯	⋯	⋯	⋯	⋯	⋯	1.57
He3	1.1343E-05	⋯	⋯	⋯	⋯	⋯	⋯	⋯	⋯	⋯	6.23E-01
He4	6.8306E-02	⋯	⋯	⋯	⋯	⋯	⋯	⋯	⋯	⋯	9.10E-01
Li6	1.1479E-10	⋯	⋯	⋯	⋯	⋯	⋯	⋯	3.00E-01	7.00E-01	⋯
Li7	1.3978E-09	⋯	⋯	⋯	⋯	⋯	⋯	⋯	3.00E-01	5.05E-01	1.95E-01
Be9	1.6640E-11	⋯	⋯	⋯	⋯	⋯	⋯	⋯	2.50E-01	7.50E-01	⋯
B10	1.0146E-10	⋯	⋯	⋯	⋯	⋯	⋯	⋯	2.50E-01	7.50E-01	⋯
B11	4.1043E-10	⋯	⋯	⋯	⋯	⋯	⋯	⋯	2.50E-01	7.50E-01	⋯
C12	1.9355E-04	⋯	⋯	⋯	⋯	⋯	1.12E-02	9.89E-01	⋯	⋯	⋯
C13	2.1747E-06	⋯	⋯	⋯	⋯	⋯	2.19E-05	1.00	⋯	⋯	⋯
N14	5.7550E-05	⋯	⋯	⋯	⋯	⋯	4.56E-06	1.00	⋯	⋯	⋯
N15	2.1158E-07	⋯	⋯	⋯	⋯	⋯	3.38E-06	1.00	⋯	⋯	⋯
O16	4.2717E-04	⋯	⋯	⋯	⋯	⋯	9.46E-03	9.91E-01	⋯	⋯	⋯
O17	1.5929E-07	⋯	⋯	⋯	⋯	⋯	6.27E-05	1.00	⋯	⋯	⋯

Table 2—Continued

Ion	Solar	Main S	Weak S	R	νP	γ	Ia	Massive	GCR	ν/Novae/GCR	BBN
O18	8.5638E-07	$\cdots$	$\cdots$	$\cdots$	$\cdots$	$\cdots$	8.13E-05	1.00	$\cdots$	$\cdots$	$\cdots$
F19	2.1877E-08	$\cdots$	$\cdots$	$\cdots$	$\cdots$	$\cdots$	4.42E-06	1.00	$\cdots$	$\cdots$	$\cdots$
Ne20	8.3148E-05	$\cdots$	$\cdots$	$\cdots$	$\cdots$	$\cdots$	8.22E-04	9.99E-01	$\cdots$	$\cdots$	$\cdots$
Ne21	1.9932E-07	$\cdots$	$\cdots$	$\cdots$	$\cdots$	$\cdots$	3.65E-03	9.96E-01	$\cdots$	$\cdots$	$\cdots$
Ne22	6.1139E-06	$\cdots$	$\cdots$	$\cdots$	$\cdots$	$\cdots$	3.81E-01	6.19E-01	$\cdots$	$\cdots$	$\cdots$
Na23	1.5705E-06	$\cdots$	$\cdots$	$\cdots$	$\cdots$	$\cdots$	5.08E-03	9.95E-01	$\cdots$	$\cdots$	$\cdots$
Mg24	2.2036E-05	$\cdots$	$\cdots$	$\cdots$	$\cdots$	$\cdots$	1.63E-02	9.84E-01	$\cdots$	$\cdots$	$\cdots$
Mg25	2.7905E-06	$\cdots$	$\cdots$	$\cdots$	$\cdots$	$\cdots$	5.23E-03	9.95E-01	$\cdots$	$\cdots$	$\cdots$
Mg26	3.0701E-06	$\cdots$	$\cdots$	$\cdots$	$\cdots$	$\cdots$	3.58E-03	9.96E-01	$\cdots$	$\cdots$	$\cdots$
Al27	2.3014E-06	$\cdots$	$\cdots$	$\cdots$	$\cdots$	$\cdots$	7.35E-02	9.26E-01	$\cdots$	$\cdots$	$\cdots$
Si28	2.5093E-05	$\cdots$	$\cdots$	$\cdots$	$\cdots$	$\cdots$	2.51E-01	7.49E-01	$\cdots$	$\cdots$	$\cdots$
Si29	1.2741E-06	$\cdots$	$\cdots$	$\cdots$	$\cdots$	$\cdots$	2.65E-01	7.35E-01	$\cdots$	$\cdots$	$\cdots$
Si30	8.3992E-07	$\cdots$	$\cdots$	$\cdots$	$\cdots$	$\cdots$	4.28E-01	5.72E-01	$\cdots$	$\cdots$	$\cdots$
P31	2.2592E-07	$\cdots$	$\cdots$	$\cdots$	$\cdots$	$\cdots$	1.73E-01	8.27E-01	$\cdots$	$\cdots$	$\cdots$
S32	1.0890E-05	$\cdots$	$\cdots$	$\cdots$	$\cdots$	$\cdots$	2.16E-01	7.84E-01	$\cdots$	$\cdots$	$\cdots$

Table 2—Continued

Ion	Solar	Main S	Weak S	R	νP	γ	Ia	Massive	GCR	ν/Novae/GCR	BBN
S33	8.5956E-08	$\cdots$	$\cdots$	$\cdots$	$\cdots$	$\cdots$	2.28E-01	7.72E-01	$\cdots$	$\cdots$	$\cdots$
S34	4.8307E-07	$\cdots$	$\cdots$	$\cdots$	$\cdots$	$\cdots$	3.93E-01	6.07E-01	$\cdots$	$\cdots$	$\cdots$
S36	1.9483E-09	$\cdots$	$\cdots$	$\cdots$	$\cdots$	$\cdots$	4.86E-01	5.14E-01	$\cdots$	$\cdots$	$\cdots$
Cl35	1.0653E-07	$\cdots$	$\cdots$	$\cdots$	$\cdots$	$\cdots$	8.18E-02	9.18E-01	$\cdots$	$\cdots$	$\cdots$
Cl37	3.4066E-08	$\cdots$	$\cdots$	$\cdots$	$\cdots$	$\cdots$	1.16E-01	8.84E-01	$\cdots$	$\cdots$	$\cdots$
Ar36	2.1329E-06	$\cdots$	$\cdots$	$\cdots$	$\cdots$	$\cdots$	2.14E-01	7.86E-01	$\cdots$	$\cdots$	$\cdots$
Ar38	3.8781E-07	$\cdots$	$\cdots$	$\cdots$	$\cdots$	$\cdots$	2.81E-01	7.19E-01	$\cdots$	$\cdots$	$\cdots$
Ar40	6.0578E-10	$\cdots$	$\cdots$	$\cdots$	$\cdots$	$\cdots$	3.98E-01	6.02E-01	$\cdots$	$\cdots$	$\cdots$
K39	9.5342E-08	$\cdots$	$\cdots$	$\cdots$	$\cdots$	$\cdots$	5.10E-02	9.49E-01	$\cdots$	$\cdots$	$\cdots$
K40	1.5000E-10	$\cdots$	$\cdots$	$\cdots$	$\cdots$	$\cdots$	$\cdots$	1.00	$\cdots$	$\cdots$	$\cdots$
K41	6.8806E-09	$\cdots$	$\cdots$	$\cdots$	$\cdots$	$\cdots$	6.07E-02	9.39E-01	$\cdots$	$\cdots$	$\cdots$
Ca40	1.5925E-06	$\cdots$	$\cdots$	$\cdots$	$\cdots$	$\cdots$	2.97E-01	7.03E-01	$\cdots$	$\cdots$	$\cdots$
Ca42	1.0629E-08	$\cdots$	$\cdots$	$\cdots$	$\cdots$	$\cdots$	1.93E-01	8.07E-01	$\cdots$	$\cdots$	$\cdots$
Ca43	2.2179E-09	$\cdots$	$\cdots$	$\cdots$	$\cdots$	$\cdots$	1.71E-02	9.83E-01	$\cdots$	$\cdots$	$\cdots$
Ca44	3.4270E-08	$\cdots$	$\cdots$	$\cdots$	$\cdots$	$\cdots$	5.79E-02	9.42E-01	$\cdots$	$\cdots$	$\cdots$

Table 2—Continued

Ion	Solar	Main S	Weak S	R	νP	γ	Ia	Massive	GCR	ν/Novae/GCR	BBN
Ca46	6.5714E-11	$\cdots$	$\cdots$	$\cdots$	$\cdots$	$\cdots$	9.58E-01	4.23E-02	$\cdots$	$\cdots$	$\cdots$
Ca48	3.0721E-09	$\cdots$	$\cdots$	$\cdots$	$\cdots$	$\cdots$	3.16E-01	6.84E-01	$\cdots$	$\cdots$	$\cdots$
Sc45	9.3722E-10	$\cdots$	$\cdots$	$\cdots$	$\cdots$	$\cdots$	3.26E-02	9.67E-01	$\cdots$	$\cdots$	$\cdots$
Ti46	5.5503E-09	$\cdots$	$\cdots$	$\cdots$	$\cdots$	$\cdots$	3.51E-01	6.49E-01	$\cdots$	$\cdots$	$\cdots$
Ti47	5.0040E-09	$\cdots$	$\cdots$	$\cdots$	$\cdots$	$\cdots$	5.00E-02	9.50E-01	$\cdots$	$\cdots$	$\cdots$
Ti48	4.9602E-08	$\cdots$	$\cdots$	$\cdots$	$\cdots$	$\cdots$	2.65E-01	7.35E-01	$\cdots$	$\cdots$	$\cdots$
Ti49	3.6394E-09	$\cdots$	$\cdots$	$\cdots$	$\cdots$	$\cdots$	3.53E-01	6.47E-01	$\cdots$	$\cdots$	$\cdots$
Ti50	3.4887E-09	$\cdots$	$\cdots$	$\cdots$	$\cdots$	$\cdots$	1.00	8.27E-05	$\cdots$	$\cdots$	$\cdots$
V50	1.9458E-11	$\cdots$	$\cdots$	$\cdots$	$\cdots$	$\cdots$	1.78E-01	8.22E-01	$\cdots$	$\cdots$	$\cdots$
V51	7.7732E-09	$\cdots$	$\cdots$	$\cdots$	$\cdots$	$\cdots$	4.23E-01	5.77E-01	$\cdots$	$\cdots$	$\cdots$
Cr50	1.5469E-08	$\cdots$	$\cdots$	$\cdots$	$\cdots$	$\cdots$	7.65E-01	2.35E-01	$\cdots$	$\cdots$	$\cdots$
Cr52	2.9829E-07	$\cdots$	$\cdots$	$\cdots$	$\cdots$	$\cdots$	5.64E-01	4.36E-01	$\cdots$	$\cdots$	$\cdots$
Cr53	3.3822E-08	$\cdots$	$\cdots$	$\cdots$	$\cdots$	$\cdots$	7.29E-01	2.71E-01	$\cdots$	$\cdots$	$\cdots$
Cr54	8.4184E-09	$\cdots$	$\cdots$	$\cdots$	$\cdots$	$\cdots$	9.91E-01	8.88E-03	$\cdots$	$\cdots$	$\cdots$
Mn55	2.5088E-07	$\cdots$	$\cdots$	$\cdots$	$\cdots$	$\cdots$	8.69E-01	1.31E-01	$\cdots$	$\cdots$	$\cdots$

Table 2—Continued

Ion	Solar	Main S	Weak S	R	νP	γ	Ia	Massive	GCR	ν/Novae/GCR	BBN
Fe54	1.3481E-06	$\cdots$	$\cdots$	$\cdots$	$\cdots$	$\cdots$	9.66E-01	3.35E-02	$\cdots$	$\cdots$	$\cdots$
Fe56	2.1162E-05	$\cdots$	$\cdots$	$\cdots$	$\cdots$	$\cdots$	6.94E-01	3.07E-01	$\cdots$	$\cdots$	$\cdots$
Fe57	4.8876E-07	$\cdots$	1.40E-04	$\cdots$	$\cdots$	$\cdots$	$\cdots$	1.00	$\cdots$	$\cdots$	$\cdots$
Fe58	6.5018E-08	$\cdots$	1.79E-02	$\cdots$	$\cdots$	$\cdots$	$\cdots$	9.82E-01	$\cdots$	$\cdots$	$\cdots$
Co59	6.3817E-08	$\cdots$	8.97E-03	$\cdots$	$\cdots$	$\cdots$	$\cdots$	9.91E-01	$\cdots$	$\cdots$	$\cdots$
Ni58	9.0816E-07	$\cdots$	$\cdots$	$\cdots$	$\cdots$	$\cdots$	$\cdots$	1.00	$\cdots$	$\cdots$	$\cdots$
Ni60	3.4988E-07	$\cdots$	3.80E-03	$\cdots$	$\cdots$	$\cdots$	$\cdots$	9.96E-01	$\cdots$	$\cdots$	$\cdots$
Ni61	1.5206E-08	$\cdots$	3.74E-02	$\cdots$	$\cdots$	$\cdots$	$\cdots$	9.63E-01	$\cdots$	$\cdots$	$\cdots$
Ni62	4.8485E-08	$\cdots$	7.33E-02	$\cdots$	$\cdots$	$\cdots$	$\cdots$	9.27E-01	$\cdots$	$\cdots$	$\cdots$
Ni64	1.2348E-08	$\cdots$	2.81E-01	$\cdots$	$\cdots$	$\cdots$	$\cdots$	7.19E-01	$\cdots$	$\cdots$	$\cdots$
Cu63	1.0184E-08	7.00E-03	1.61E-01	$\cdots$	$\cdots$	$\cdots$	$\cdots$	8.32E-01	$\cdots$	$\cdots$	$\cdots$
Cu65	4.5381E-09	1.90E-02	7.27E-01	$\cdots$	$\cdots$	$\cdots$	$\cdots$	2.54E-01	$\cdots$	$\cdots$	$\cdots$
Zn64	1.7153E-08	1.00E-03	6.67E-02	$\cdots$	$\cdots$	$\cdots$	$\cdots$	9.32E-01	$\cdots$	$\cdots$	$\cdots$
Zn66	9.8409E-09	9.00E-03	2.70E-01	$\cdots$	$\cdots$	$\cdots$	$\cdots$	7.21E-01	$\cdots$	$\cdots$	$\cdots$
Zn67	1.4461E-09	1.40E-02	4.08E-01	$\cdots$	$\cdots$	$\cdots$	$\cdots$	5.78E-01	$\cdots$	$\cdots$	$\cdots$

Table 2—Continued

Ion	Solar	Main S	Weak S	R	νP	γ	Ia	Massive	GCR	ν/Novae/GCR	BBN
Zn68	6.6135E-09	2.00E-02	5.19E-01	$\cdots$	$\cdots$	$\cdots$	$\cdots$	4.61E-01	$\cdots$	$\cdots$	$\cdots$
Zn70	2.1869E-10	1.00E-03	$\cdots$	9.99E-01	$\cdots$	$\cdots$	$\cdots$	$\cdots$	$\cdots$	$\cdots$	$\cdots$
Ga69	5.9779E-10	3.20E-02	7.41E-01	2.27E-01	$\cdots$	$\cdots$	$\cdots$	$\cdots$	$\cdots$	$\cdots$	$\cdots$
Ga71	3.9674E-10	5.30E-02	9.47E-01	$\cdots$	$\cdots$	$\cdots$	$\cdots$	$\cdots$	$\cdots$	$\cdots$	$\cdots$
Ge70	6.6233E-10	5.40E-02	9.46E-01	$\cdots$	$\cdots$	$\cdots$	$\cdots$	$\cdots$	$\cdots$	$\cdots$	$\cdots$
Ge72	8.6283E-10	7.00E-02	6.80E-01	2.50E-01	$\cdots$	$\cdots$	$\cdots$	$\cdots$	$\cdots$	$\cdots$	$\cdots$
Ge73	2.4071E-10	6.70E-02	6.88E-01	2.45E-01	$\cdots$	$\cdots$	$\cdots$	$\cdots$	$\cdots$	$\cdots$	$\cdots$
Ge74	1.1211E-09	8.10E-02	6.73E-01	2.46E-01	$\cdots$	$\cdots$	$\cdots$	$\cdots$	$\cdots$	$\cdots$	$\cdots$
Ge76	2.3219E-10	1.00E-03	$\cdots$	9.99E-01	$\cdots$	$\cdots$	$\cdots$	$\cdots$	$\cdots$	$\cdots$	$\cdots$
As75	1.6585E-10	5.50E-02	4.47E-01	4.98E-01	$\cdots$	$\cdots$	$\cdots$	$\cdots$	$\cdots$	$\cdots$	$\cdots$
Se74	1.6322E-11	$\cdots$	5.00E-01	$\cdots$	5.00E-01	$\cdots$	$\cdots$	$\cdots$	$\cdots$	$\cdots$	$\cdots$
Se76	1.7196E-10	1.45E-01	8.55E-01	$\cdots$	$\cdots$	$\cdots$	$\cdots$	$\cdots$	$\cdots$	$\cdots$	$\cdots$
Se77	1.4018E-10	6.80E-02	3.91E-01	5.41E-01	$\cdots$	$\cdots$	$\cdots$	$\cdots$	$\cdots$	$\cdots$	$\cdots$
Se78	4.3645E-10	1.53E-01	6.58E-01	1.89E-01	$\cdots$	$\cdots$	$\cdots$	$\cdots$	$\cdots$	$\cdots$	$\cdots$
Se80	9.1077E-10	8.90E-02	9.14E-03	9.02E-01	$\cdots$	$\cdots$	$\cdots$	$\cdots$	$\cdots$	$\cdots$	$\cdots$

Table 2—Continued

Ion	Solar	Main S	Weak S	R	νP	γ	Ia	Massive	GCR	ν/Novae/GCR	BBN
Se82	1.6030E-10	1.00E-03	$\cdots$	9.99E-01	$\cdots$	$\cdots$	$\cdots$	$\cdots$	$\cdots$	$\cdots$	$\cdots$
Br79	1.4768E-10	7.40E-02	1.78E-01	7.48E-01	$\cdots$	$\cdots$	$\cdots$	$\cdots$	$\cdots$	$\cdots$	$\cdots$
Br81	1.4368E-10	9.30E-02	3.99E-01	5.08E-01	$\cdots$	$\cdots$	$\cdots$	$\cdots$	$\cdots$	$\cdots$	$\cdots$
Kr78	5.5028E-12	$\cdots$	5.00E-01	$\cdots$	5.00E-01	$\cdots$	$\cdots$	$\cdots$	$\cdots$	$\cdots$	$\cdots$
Kr80	3.5341E-11	9.80E-02	7.52E-01	$\cdots$	1.50E-01	$\cdots$	$\cdots$	$\cdots$	$\cdots$	$\cdots$	$\cdots$
Kr82	1.7707E-10	2.87E-01	6.83E-01	$\cdots$	3.00E-02	$\cdots$	$\cdots$	$\cdots$	$\cdots$	$\cdots$	$\cdots$
Kr83	1.7542E-10	1.07E-01	2.56E-01	6.37E-01	$\cdots$	$\cdots$	$\cdots$	$\cdots$	$\cdots$	$\cdots$	$\cdots$
Kr84	8.6451E-10	1.38E-01	1.71E-01	6.91E-01	$\cdots$	$\cdots$	$\cdots$	$\cdots$	$\cdots$	$\cdots$	$\cdots$
Kr86	2.6143E-10	1.89E-01	$\cdots$	8.11E-01	$\cdots$	$\cdots$	$\cdots$	$\cdots$	$\cdots$	$\cdots$	$\cdots$
Rb85	1.3932E-10	1.75E-01	3.16E-01	5.09E-01	$\cdots$	$\cdots$	$\cdots$	$\cdots$	$\cdots$	$\cdots$	$\cdots$
Rb87	5.7339E-11	2.80E-01	$\cdots$	7.20E-01	$\cdots$	$\cdots$	$\cdots$	$\cdots$	$\cdots$	$\cdots$	$\cdots$
Sr84	3.5322E-12	$\cdots$	5.00E-01	$\cdots$	5.00E-01	$\cdots$	$\cdots$	$\cdots$	$\cdots$	$\cdots$	$\cdots$
Sr86	6.2461E-11	5.60E-01	4.40E-01	$\cdots$	$\cdots$	$\cdots$	$\cdots$	$\cdots$	$\cdots$	$\cdots$	$\cdots$
Sr87	4.3651E-11	5.53E-01	4.47E-01	$\cdots$	$\cdots$	$\cdots$	$\cdots$	$\cdots$	$\cdots$	$\cdots$	$\cdots$
Sr88	5.2333E-10	1.00	$\cdots$	$\cdots$	$\cdots$	$\cdots$	$\cdots$	$\cdots$	$\cdots$	$\cdots$	$\cdots$

Table 2—Continued

Ion	Solar	Main S	Weak S	R	νP	γ	Ia	Massive	GCR	ν/Novae/GCR	BBN
Y89	1.2610E-10	9.81E-01	1.90E-02	$\cdots$	$\cdots$	$\cdots$	$\cdots$	$\cdots$	$\cdots$	$\cdots$	$\cdots$
Zr90	1.5089E-10	7.65E-01	1.49E-02	2.20E-01	$\cdots$	$\cdots$	$\cdots$	$\cdots$	$\cdots$	$\cdots$	$\cdots$
Zr91	3.2913E-11	9.52E-01	1.27E-02	3.53E-02	$\cdots$	$\cdots$	$\cdots$	$\cdots$	$\cdots$	$\cdots$	$\cdots$
Zr92	5.0282E-11	9.05E-01	6.81E-03	8.82E-02	$\cdots$	$\cdots$	$\cdots$	$\cdots$	$\cdots$	$\cdots$	$\cdots$
Zr94	5.0969E-11	1.00	$\cdots$	$\cdots$	$\cdots$	$\cdots$	$\cdots$	$\cdots$	$\cdots$	$\cdots$	$\cdots$
Zr96	8.2083E-12	4.63E-01	$\cdots$	5.37E-01	$\cdots$	$\cdots$	$\cdots$	$\cdots$	$\cdots$	$\cdots$	$\cdots$
Nb93	2.1209E-11	9.14E-01	3.37E-03	8.26E-02	$\cdots$	$\cdots$	$\cdots$	$\cdots$	$\cdots$	$\cdots$	$\cdots$
Mo92	1.0075E-11	$\cdots$	$\cdots$	$\cdots$	1.00	$\cdots$	$\cdots$	$\cdots$	$\cdots$	$\cdots$	$\cdots$
Mo94	6.3478E-12	8.00E-03	$\cdots$	$\cdots$	9.92E-01	$\cdots$	$\cdots$	$\cdots$	$\cdots$	$\cdots$	$\cdots$
Mo95	1.0986E-11	6.61E-01	3.59E-03	3.35E-01	$\cdots$	$\cdots$	$\cdots$	$\cdots$	$\cdots$	$\cdots$	$\cdots$
Mo96	1.1564E-11	1.00	$\cdots$	$\cdots$	$\cdots$	$\cdots$	$\cdots$	$\cdots$	$\cdots$	$\cdots$	$\cdots$
Mo97	6.6583E-12	6.11E-01	5.55E-03	3.83E-01	$\cdots$	$\cdots$	$\cdots$	$\cdots$	$\cdots$	$\cdots$	$\cdots$
Mo98	1.6919E-11	7.94E-01	8.62E-03	1.97E-01	$\cdots$	$\cdots$	$\cdots$	$\cdots$	$\cdots$	$\cdots$	$\cdots$
Mo100	6.8143E-12	4.30E-02	$\cdots$	9.57E-01	$\cdots$	$\cdots$	$\cdots$	$\cdots$	$\cdots$	$\cdots$	$\cdots$
Ru96	2.6864E-12	$\cdots$	$\cdots$	$\cdots$	1.00	$\cdots$	$\cdots$	$\cdots$	$\cdots$	$\cdots$	$\cdots$

Table 2—Continued

Ion	Solar	Main S	Weak S	R	νP	γ	Ia	Massive	GCR	ν/Novae/GCR	BBN
Ru98	9.0586E-13	$\cdots$	$\cdots$	$\cdots$	1.00	$\cdots$	$\cdots$	$\cdots$	$\cdots$	$\cdots$	$\cdots$
Ru99	6.1841E-12	3.04E-01	3.65E-03	6.92E-01	$\cdots$	$\cdots$	$\cdots$	$\cdots$	$\cdots$	$\cdots$	$\cdots$
Ru100	6.1068E-12	1.00	$\cdots$	$\cdots$	$\cdots$	$\cdots$	$\cdots$	$\cdots$	$\cdots$	$\cdots$	$\cdots$
Ru101	8.2694E-12	1.63E-01	2.31E-03	8.35E-01	$\cdots$	$\cdots$	$\cdots$	$\cdots$	$\cdots$	$\cdots$	$\cdots$
Ru102	1.5294E-11	4.57E-01	$\cdots$	5.43E-01	$\cdots$	$\cdots$	$\cdots$	$\cdots$	$\cdots$	$\cdots$	$\cdots$
Ru104	9.0261E-12	2.20E-02	$\cdots$	9.78E-01	$\cdots$	$\cdots$	$\cdots$	$\cdots$	$\cdots$	$\cdots$	$\cdots$
Rh103	1.0078E-11	1.57E-01	$\cdots$	8.43E-01	$\cdots$	$\cdots$	$\cdots$	$\cdots$	$\cdots$	$\cdots$	$\cdots$
Pd102	3.7684E-13	$\cdots$	$\cdots$	$\cdots$	2.50E-01	7.50E-01	$\cdots$	$\cdots$	$\cdots$	$\cdots$	$\cdots$
Pd104	4.1157E-12	1.00	$\cdots$	$\cdots$	$\cdots$	$\cdots$	$\cdots$	$\cdots$	$\cdots$	$\cdots$	$\cdots$
Pd105	8.2499E-12	1.46E-01	$\cdots$	8.54E-01	$\cdots$	$\cdots$	$\cdots$	$\cdots$	$\cdots$	$\cdots$	$\cdots$
Pd106	1.0097E-11	5.45E-01	$\cdots$	4.55E-01	$\cdots$	$\cdots$	$\cdots$	$\cdots$	$\cdots$	$\cdots$	$\cdots$
Pd108	9.7757E-12	6.95E-01	$\cdots$	3.05E-01	$\cdots$	$\cdots$	$\cdots$	$\cdots$	$\cdots$	$\cdots$	$\cdots$
Pd110	4.3300E-12	2.80E-02	$\cdots$	9.72E-01	$\cdots$	$\cdots$	$\cdots$	$\cdots$	$\cdots$	$\cdots$	$\cdots$
Ag107	6.8982E-12	1.59E-01	$\cdots$	8.41E-01	$\cdots$	$\cdots$	$\cdots$	$\cdots$	$\cdots$	$\cdots$	$\cdots$
Ag109	6.4087E-12	2.71E-01	$\cdots$	7.29E-01	$\cdots$	$\cdots$	$\cdots$	$\cdots$	$\cdots$	$\cdots$	$\cdots$

Table 2—Continued

Ion	Solar	Main S	Weak S	R	νP	γ	Ia	Massive	GCR	ν/Novae/GCR	BBN
Cd106	5.3522E-13	$\cdots$	$\cdots$	$\cdots$	$\cdots$	1.00	$\cdots$	$\cdots$	$\cdots$	$\cdots$	$\cdots$
Cd108	3.8108E-13	4.00E-03	$\cdots$	$\cdots$	$\cdots$	9.96E-01	$\cdots$	$\cdots$	$\cdots$	$\cdots$	$\cdots$
Cd110	5.3479E-12	1.00	$\cdots$	$\cdots$	$\cdots$	$\cdots$	$\cdots$	$\cdots$	$\cdots$	$\cdots$	$\cdots$
Cd111	5.4807E-12	3.54E-01	$\cdots$	6.46E-01	$\cdots$	$\cdots$	$\cdots$	$\cdots$	$\cdots$	$\cdots$	$\cdots$
Cd112	1.0332E-11	7.00E-01	$\cdots$	3.00E-01	$\cdots$	$\cdots$	$\cdots$	$\cdots$	$\cdots$	$\cdots$	$\cdots$
Cd113	5.2323E-12	4.02E-01	$\cdots$	5.98E-01	$\cdots$	$\cdots$	$\cdots$	$\cdots$	$\cdots$	$\cdots$	$\cdots$
Cd114	1.2302E-11	8.37E-01	$\cdots$	1.63E-01	$\cdots$	$\cdots$	$\cdots$	$\cdots$	$\cdots$	$\cdots$	$\cdots$
Cd116	3.2070E-12	1.58E-01	$\cdots$	8.42E-01	$\cdots$	$\cdots$	$\cdots$	$\cdots$	$\cdots$	$\cdots$	$\cdots$
In113	2.0749E-13	$\cdots$	$\cdots$	$\cdots$	$\cdots$	1.00	$\cdots$	$\cdots$	$\cdots$	$\cdots$	$\cdots$
In115	4.6314E-12	4.09E-01	$\cdots$	5.91E-01	$\cdots$	$\cdots$	$\cdots$	$\cdots$	$\cdots$	$\cdots$	$\cdots$
Sn112	9.5212E-13	$\cdots$	$\cdots$	$\cdots$	$\cdots$	1.00	$\cdots$	$\cdots$	$\cdots$	$\cdots$	$\cdots$
Sn114	6.4619E-13	$\cdots$	$\cdots$	$\cdots$	$\cdots$	1.00	$\cdots$	$\cdots$	$\cdots$	$\cdots$	$\cdots$
Sn115	3.3241E-13	2.50E-02	$\cdots$	$\cdots$	$\cdots$	9.75E-01	$\cdots$	$\cdots$	$\cdots$	$\cdots$	$\cdots$
Sn116	1.4253E-11	1.00	$\cdots$	$\cdots$	$\cdots$	$\cdots$	$\cdots$	$\cdots$	$\cdots$	$\cdots$	$\cdots$
Sn117	7.5268E-12	5.14E-01	$\cdots$	4.86E-01	$\cdots$	$\cdots$	$\cdots$	$\cdots$	$\cdots$	$\cdots$	$\cdots$

Table 2—Continued

Ion	Solar	Main S	Weak S	R	νP	γ	Ia	Massive	GCR	ν/Novae/GCR	BBN
Sn118	2.3752E-11	7.27E-01	$\cdots$	2.73E-01	$\cdots$	$\cdots$	$\cdots$	$\cdots$	$\cdots$	$\cdots$	$\cdots$
Sn119	8.4181E-12	5.88E-01	$\cdots$	4.12E-01	$\cdots$	$\cdots$	$\cdots$	$\cdots$	$\cdots$	$\cdots$	$\cdots$
Sn120	3.1959E-11	7.62E-01	$\cdots$	2.38E-01	$\cdots$	$\cdots$	$\cdots$	$\cdots$	$\cdots$	$\cdots$	$\cdots$
Sn122	4.5390E-12	4.20E-01	$\cdots$	5.80E-01	$\cdots$	$\cdots$	$\cdots$	$\cdots$	$\cdots$	$\cdots$	$\cdots$
Sn124	5.6765E-12	$\cdots$	$\cdots$	1.00	$\cdots$	$\cdots$	$\cdots$	$\cdots$	$\cdots$	$\cdots$	$\cdots$
Sb121	4.8656E-12	3.99E-01	$\cdots$	6.01E-01	$\cdots$	$\cdots$	$\cdots$	$\cdots$	$\cdots$	$\cdots$	$\cdots$
Sb123	3.6387E-12	6.30E-02	$\cdots$	9.37E-01	$\cdots$	$\cdots$	$\cdots$	$\cdots$	$\cdots$	$\cdots$	$\cdots$
Te120	1.2251E-13	$\cdots$	$\cdots$	$\cdots$	$\cdots$	1.00	$\cdots$	$\cdots$	$\cdots$	$\cdots$	$\cdots$
Te122	3.3219E-12	1.00	$\cdots$	$\cdots$	$\cdots$	$\cdots$	$\cdots$	$\cdots$	$\cdots$	$\cdots$	$\cdots$
Te123	1.1588E-12	1.00	$\cdots$	$\cdots$	$\cdots$	$\cdots$	$\cdots$	$\cdots$	$\cdots$	$\cdots$	$\cdots$
Te124	6.1460E-12	1.00	$\cdots$	$\cdots$	$\cdots$	$\cdots$	$\cdots$	$\cdots$	$\cdots$	$\cdots$	$\cdots$
Te125	9.1106E-12	2.08E-01	$\cdots$	7.92E-01	$\cdots$	$\cdots$	$\cdots$	$\cdots$	$\cdots$	$\cdots$	$\cdots$
Te126	2.4186E-11	4.20E-01	$\cdots$	5.80E-01	$\cdots$	$\cdots$	$\cdots$	$\cdots$	$\cdots$	$\cdots$	$\cdots$
Te128	4.0438E-11	3.60E-02	$\cdots$	9.64E-01	$\cdots$	$\cdots$	$\cdots$	$\cdots$	$\cdots$	$\cdots$	$\cdots$
Te130	4.3133E-11	$\cdots$	$\cdots$	1.00	$\cdots$	$\cdots$	$\cdots$	$\cdots$	$\cdots$	$\cdots$	$\cdots$

Table 2—Continued

Ion	Solar	Main S	Weak S	R	νP	γ	Ia	Massive	GCR	ν/Novae/GCR	BBN
I127	2.9825E-11	5.50E-02	$\cdots$	9.45E-01	$\cdots$	$\cdots$	$\cdots$	$\cdots$	$\cdots$	$\cdots$	$\cdots$
Xe124	1.9108E-13	$\cdots$	$\cdots$	$\cdots$	$\cdots$	1.00	$\cdots$	$\cdots$	$\cdots$	$\cdots$	$\cdots$
Xe126	1.6569E-13	$\cdots$	$\cdots$	$\cdots$	$\cdots$	1.00	$\cdots$	$\cdots$	$\cdots$	$\cdots$	$\cdots$
Xe128	3.3162E-12	1.00	$\cdots$	$\cdots$	$\cdots$	$\cdots$	$\cdots$	$\cdots$	$\cdots$	$\cdots$	$\cdots$
Xe129	4.0773E-11	3.20E-02	$\cdots$	9.68E-01	$\cdots$	$\cdots$	$\cdots$	$\cdots$	$\cdots$	$\cdots$	$\cdots$
Xe130	6.4998E-12	1.00	$\cdots$	$\cdots$	$\cdots$	$\cdots$	$\cdots$	$\cdots$	$\cdots$	$\cdots$	$\cdots$
Xe131	3.2369E-11	7.40E-02	$\cdots$	9.26E-01	$\cdots$	$\cdots$	$\cdots$	$\cdots$	$\cdots$	$\cdots$	$\cdots$
Xe132	3.9129E-11	3.00E-01	$\cdots$	7.00E-01	$\cdots$	$\cdots$	$\cdots$	$\cdots$	$\cdots$	$\cdots$	$\cdots$
Xe134	1.4344E-11	4.00E-02	$\cdots$	9.60E-01	$\cdots$	$\cdots$	$\cdots$	$\cdots$	$\cdots$	$\cdots$	$\cdots$
Xe136	1.1681E-11	$\cdots$	$\cdots$	1.00	$\cdots$	$\cdots$	$\cdots$	$\cdots$	$\cdots$	$\cdots$	$\cdots$
Cs133	1.0102E-11	1.49E-01	$\cdots$	8.51E-01	$\cdots$	$\cdots$	$\cdots$	$\cdots$	$\cdots$	$\cdots$	$\cdots$
Ba130	1.2868E-13	$\cdots$	$\cdots$	$\cdots$	$\cdots$	1.00	$\cdots$	$\cdots$	$\cdots$	$\cdots$	$\cdots$
Ba132	1.2309E-13	$\cdots$	$\cdots$	$\cdots$	$\cdots$	1.00	$\cdots$	$\cdots$	$\cdots$	$\cdots$	$\cdots$
Ba134	2.9398E-12	1.00	$\cdots$	$\cdots$	$\cdots$	$\cdots$	$\cdots$	$\cdots$	$\cdots$	$\cdots$	$\cdots$
Ba135	8.0178E-12	2.87E-01	$\cdots$	7.13E-01	$\cdots$	$\cdots$	$\cdots$	$\cdots$	$\cdots$	$\cdots$	$\cdots$

Table 2—Continued

Ion	Solar	Main S	Weak S	R	νP	γ	Ia	Massive	GCR	ν/Novae/GCR	BBN
Ba136	9.5515E-12	1.00	⋯	⋯	⋯	⋯	⋯	⋯	⋯	⋯	⋯
Ba137	1.3661E-11	6.41E-01	⋯	3.59E-01	⋯	⋯	⋯	⋯	⋯	⋯	⋯
Ba138	8.7207E-11	8.95E-01	⋯	1.05E-01	⋯	⋯	⋯	⋯	⋯	⋯	⋯
La138	1.1371E-14	⋯	⋯	⋯	⋯	1.00	⋯	⋯	⋯	⋯	⋯
La139	1.2430E-11	6.96E-01	⋯	3.04E-01	⋯	⋯	⋯	⋯	⋯	⋯	⋯
Ce136	5.9690E-14	⋯	⋯	⋯	⋯	1.00	⋯	⋯	⋯	⋯	⋯
Ce138	8.0227E-14	⋯	⋯	⋯	⋯	1.00	⋯	⋯	⋯	⋯	⋯
Ce140	2.8385E-11	8.87E-01	⋯	1.13E-01	⋯	⋯	⋯	⋯	⋯	⋯	⋯
Ce142	3.5666E-12	1.92E-01	⋯	8.08E-01	⋯	⋯	⋯	⋯	⋯	⋯	⋯
Pr141	4.6912E-12	5.08E-01	⋯	4.92E-01	⋯	⋯	⋯	⋯	⋯	⋯	⋯
Nd142	6.2977E-12	1.00	⋯	⋯	⋯	⋯	⋯	⋯	⋯	⋯	⋯
Nd143	2.7997E-12	3.22E-01	⋯	6.78E-01	⋯	⋯	⋯	⋯	⋯	⋯	⋯
Nd144	5.5255E-12	5.13E-01	⋯	4.87E-01	⋯	⋯	⋯	⋯	⋯	⋯	⋯
Nd145	2.0265E-12	2.74E-01	⋯	7.26E-01	⋯	⋯	⋯	⋯	⋯	⋯	⋯
Nd146	3.9348E-12	6.47E-01	⋯	3.53E-01	⋯	⋯	⋯	⋯	⋯	⋯	⋯

Table 2—Continued

Ion	Solar	Main S	Weak S	R	νP	γ	Ia	Massive	GCR	ν/Novae/GCR	BBN
Nd148	1.3132E-12	1.88E-01	$\cdots$	8.12E-01	$\cdots$	$\cdots$	$\cdots$	$\cdots$	$\cdots$	$\cdots$	$\cdots$
Nd150	1.3482E-12	$\cdots$	$\cdots$	1.00	$\cdots$	$\cdots$	$\cdots$	$\cdots$	$\cdots$	$\cdots$	$\cdots$
Sm144	2.2234E-13	$\cdots$	$\cdots$	$\cdots$	$\cdots$	1.00	$\cdots$	$\cdots$	$\cdots$	$\cdots$	$\cdots$
Sm147	1.1171E-12	2.57E-01	$\cdots$	7.43E-01	$\cdots$	$\cdots$	$\cdots$	$\cdots$	$\cdots$	$\cdots$	$\cdots$
Sm148	8.1212E-13	1.00	$\cdots$	$\cdots$	$\cdots$	$\cdots$	$\cdots$	$\cdots$	$\cdots$	$\cdots$	$\cdots$
Sm149	9.9837E-13	1.25E-01	$\cdots$	8.75E-01	$\cdots$	$\cdots$	$\cdots$	$\cdots$	$\cdots$	$\cdots$	$\cdots$
Sm150	5.3059E-13	1.00	$\cdots$	$\cdots$	$\cdots$	$\cdots$	$\cdots$	$\cdots$	$\cdots$	$\cdots$	$\cdots$
Sm152	1.9303E-12	2.27E-01	$\cdots$	7.73E-01	$\cdots$	$\cdots$	$\cdots$	$\cdots$	$\cdots$	$\cdots$	$\cdots$
Sm154	1.6408E-12	2.70E-02	$\cdots$	9.73E-01	$\cdots$	$\cdots$	$\cdots$	$\cdots$	$\cdots$	$\cdots$	$\cdots$
Eu151	1.2804E-12	5.80E-02	$\cdots$	9.42E-01	$\cdots$	$\cdots$	$\cdots$	$\cdots$	$\cdots$	$\cdots$	$\cdots$
Eu153	1.3977E-12	5.70E-02	$\cdots$	9.43E-01	$\cdots$	$\cdots$	$\cdots$	$\cdots$	$\cdots$	$\cdots$	$\cdots$
Gd152	1.9865E-14	7.14E-01	$\cdots$	$\cdots$	$\cdots$	2.86E-01	$\cdots$	$\cdots$	$\cdots$	$\cdots$	$\cdots$
Gd154	2.1352E-13	1.00	$\cdots$	$\cdots$	$\cdots$	$\cdots$	$\cdots$	$\cdots$	$\cdots$	$\cdots$	$\cdots$
Gd155	1.4490E-12	5.90E-02	$\cdots$	9.41E-01	$\cdots$	$\cdots$	$\cdots$	$\cdots$	$\cdots$	$\cdots$	$\cdots$
Gd156	2.0038E-12	1.75E-01	$\cdots$	8.25E-01	$\cdots$	$\cdots$	$\cdots$	$\cdots$	$\cdots$	$\cdots$	$\cdots$

Table 2—Continued

Ion	Solar	Main S	Weak S	R	νP	γ	Ia	Massive	GCR	ν/Novae/GCR	BBN
Gd157	1.5324E-12	1.11E-01	$\cdots$	8.89E-01	$\cdots$	$\cdots$	$\cdots$	$\cdots$	$\cdots$	$\cdots$	$\cdots$
Gd158	2.4315E-12	2.82E-01	$\cdots$	7.18E-01	$\cdots$	$\cdots$	$\cdots$	$\cdots$	$\cdots$	$\cdots$	$\cdots$
Gd160	2.1406E-12	6.00E-03	$\cdots$	9.94E-01	$\cdots$	$\cdots$	$\cdots$	$\cdots$	$\cdots$	$\cdots$	$\cdots$
Tb159	1.7255E-12	8.50E-02	$\cdots$	9.15E-01	$\cdots$	$\cdots$	$\cdots$	$\cdots$	$\cdots$	$\cdots$	$\cdots$
Dy156	6.1493E-15	$\cdots$	$\cdots$	$\cdots$	$\cdots$	1.00	$\cdots$	$\cdots$	$\cdots$	$\cdots$	$\cdots$
Dy158	1.0432E-14	$\cdots$	$\cdots$	$\cdots$	$\cdots$	1.00	$\cdots$	$\cdots$	$\cdots$	$\cdots$	$\cdots$
Dy160	2.5575E-13	1.00	$\cdots$	$\cdots$	$\cdots$	$\cdots$	$\cdots$	$\cdots$	$\cdots$	$\cdots$	$\cdots$
Dy161	2.0742E-12	5.10E-02	$\cdots$	9.49E-01	$\cdots$	$\cdots$	$\cdots$	$\cdots$	$\cdots$	$\cdots$	$\cdots$
Dy162	2.7974E-12	1.56E-01	$\cdots$	8.44E-01	$\cdots$	$\cdots$	$\cdots$	$\cdots$	$\cdots$	$\cdots$	$\cdots$
Dy163	2.7338E-12	4.20E-02	$\cdots$	9.58E-01	$\cdots$	$\cdots$	$\cdots$	$\cdots$	$\cdots$	$\cdots$	$\cdots$
Dy164	3.1032E-12	2.26E-01	$\cdots$	7.74E-01	$\cdots$	$\cdots$	$\cdots$	$\cdots$	$\cdots$	$\cdots$	$\cdots$
Ho165	2.4767E-12	8.00E-02	$\cdots$	9.20E-01	$\cdots$	$\cdots$	$\cdots$	$\cdots$	$\cdots$	$\cdots$	$\cdots$
Er162	9.8904E-15	$\cdots$	$\cdots$	$\cdots$	$\cdots$	1.00	$\cdots$	$\cdots$	$\cdots$	$\cdots$	$\cdots$
Er164	1.1392E-13	7.40E-01	$\cdots$	$\cdots$	$\cdots$	2.60E-01	$\cdots$	$\cdots$	$\cdots$	$\cdots$	$\cdots$
Er166	2.3839E-12	1.59E-01	$\cdots$	8.41E-01	$\cdots$	$\cdots$	$\cdots$	$\cdots$	$\cdots$	$\cdots$	$\cdots$

Table 2—Continued

Ion	Solar	Main S	Weak S	R	νP	γ	Ia	Massive	GCR	ν/Novae/GCR	BBN
Er167	1.6272E-12	9.10E-02	$\cdots$	9.09E-01	$\cdots$	$\cdots$	$\cdots$	$\cdots$	$\cdots$	$\cdots$	$\cdots$
Er168	1.9196E-12	2.89E-01	$\cdots$	7.11E-01	$\cdots$	$\cdots$	$\cdots$	$\cdots$	$\cdots$	$\cdots$	$\cdots$
Er170	1.0609E-12	1.23E-01	$\cdots$	8.77E-01	$\cdots$	$\cdots$	$\cdots$	$\cdots$	$\cdots$	$\cdots$	$\cdots$
Tm169	1.1033E-12	1.25E-01	$\cdots$	8.75E-01	$\cdots$	$\cdots$	$\cdots$	$\cdots$	$\cdots$	$\cdots$	$\cdots$
Yb168	8.5919E-15	$\cdots$	$\cdots$	$\cdots$	$\cdots$	1.00	$\cdots$	$\cdots$	$\cdots$	$\cdots$	$\cdots$
Yb170	2.0796E-13	1.00	$\cdots$	$\cdots$	$\cdots$	$\cdots$	$\cdots$	$\cdots$	$\cdots$	$\cdots$	$\cdots$
Yb171	9.8235E-13	2.03E-01	$\cdots$	7.97E-01	$\cdots$	$\cdots$	$\cdots$	$\cdots$	$\cdots$	$\cdots$	$\cdots$
Yb172	1.5124E-12	4.29E-01	$\cdots$	5.71E-01	$\cdots$	$\cdots$	$\cdots$	$\cdots$	$\cdots$	$\cdots$	$\cdots$
Yb173	1.1230E-12	2.65E-01	$\cdots$	7.35E-01	$\cdots$	$\cdots$	$\cdots$	$\cdots$	$\cdots$	$\cdots$	$\cdots$
Yb174	2.2334E-12	6.02E-01	$\cdots$	3.98E-01	$\cdots$	$\cdots$	$\cdots$	$\cdots$	$\cdots$	$\cdots$	$\cdots$
Yb176	9.0626E-13	8.30E-02	$\cdots$	9.17E-01	$\cdots$	$\cdots$	$\cdots$	$\cdots$	$\cdots$	$\cdots$	$\cdots$
Lu175	1.0058E-12	1.77E-01	$\cdots$	8.23E-01	$\cdots$	$\cdots$	$\cdots$	$\cdots$	$\cdots$	$\cdots$	$\cdots$
Lu176	2.9191E-14	1.00	$\cdots$	$\cdots$	$\cdots$	$\cdots$	$\cdots$	$\cdots$	$\cdots$	$\cdots$	$\cdots$
Hf174	6.8707E-15	$\cdots$	$\cdots$	$\cdots$	$\cdots$	1.00	$\cdots$	$\cdots$	$\cdots$	$\cdots$	$\cdots$
Hf176	2.2066E-13	1.00	$\cdots$	$\cdots$	$\cdots$	$\cdots$	$\cdots$	$\cdots$	$\cdots$	$\cdots$	$\cdots$

Table 2—Continued

Ion	Solar	Main S	Weak S	R	νP	γ	Ia	Massive	GCR	ν/Novae/GCR	BBN
Hf177	7.8866E-13	1.66E-01	$\cdots$	8.34E-01	$\cdots$	$\cdots$	$\cdots$	$\cdots$	$\cdots$	$\cdots$	$\cdots$
Hf178	1.1570E-12	5.66E-01	$\cdots$	4.34E-01	$\cdots$	$\cdots$	$\cdots$	$\cdots$	$\cdots$	$\cdots$	$\cdots$
Hf179	5.7769E-13	3.96E-01	$\cdots$	6.04E-01	$\cdots$	$\cdots$	$\cdots$	$\cdots$	$\cdots$	$\cdots$	$\cdots$
Hf180	1.4878E-12	8.57E-01	$\cdots$	1.43E-01	$\cdots$	$\cdots$	$\cdots$	$\cdots$	$\cdots$	$\cdots$	$\cdots$
Ta180	7.0387E-17	$\cdots$	$\cdots$	$\cdots$	$\cdots$	1.00	$\cdots$	$\cdots$	$\cdots$	$\cdots$	$\cdots$
Ta181	5.7218E-13	4.51E-01	$\cdots$	5.49E-01	$\cdots$	$\cdots$	$\cdots$	$\cdots$	$\cdots$	$\cdots$	$\cdots$
W180	4.4674E-15	$\cdots$	$\cdots$	$\cdots$	$\cdots$	1.00	$\cdots$	$\cdots$	$\cdots$	$\cdots$	$\cdots$
W182	9.8815E-13	6.01E-01	$\cdots$	3.99E-01	$\cdots$	$\cdots$	$\cdots$	$\cdots$	$\cdots$	$\cdots$	$\cdots$
W183	5.3377E-13	5.70E-01	$\cdots$	4.30E-01	$\cdots$	$\cdots$	$\cdots$	$\cdots$	$\cdots$	$\cdots$	$\cdots$
W184	1.1427E-12	7.64E-01	$\cdots$	2.36E-01	$\cdots$	$\cdots$	$\cdots$	$\cdots$	$\cdots$	$\cdots$	$\cdots$
W186	1.0600E-12	5.74E-01	$\cdots$	4.26E-01	$\cdots$	$\cdots$	$\cdots$	$\cdots$	$\cdots$	$\cdots$	$\cdots$
Re185	5.6366E-13	2.81E-01	$\cdots$	7.19E-01	$\cdots$	$\cdots$	$\cdots$	$\cdots$	$\cdots$	$\cdots$	$\cdots$
Re187	1.0169E-12	1.02E-01	$\cdots$	8.98E-01	$\cdots$	$\cdots$	$\cdots$	$\cdots$	$\cdots$	$\cdots$	$\cdots$
Os184	3.6631E-15	$\cdots$	$\cdots$	$\cdots$	$\cdots$	1.00	$\cdots$	$\cdots$	$\cdots$	$\cdots$	$\cdots$
Os186	2.9457E-13	1.00	$\cdots$	$\cdots$	$\cdots$	$\cdots$	$\cdots$	$\cdots$	$\cdots$	$\cdots$	$\cdots$

Table 2—Continued

Ion	Solar	Main S	Weak S	R	νP	γ	Ia	Massive	GCR	ν/Novae/GCR	BBN
Os187	2.3429E-13	4.06E-01	$\cdots$	$\cdots$	$\cdots$	5.94E-01	$\cdots$	$\cdots$	$\cdots$	$\cdots$	$\cdots$
Os188	2.4584E-12	2.85E-01	$\cdots$	7.15E-01	$\cdots$	$\cdots$	$\cdots$	$\cdots$	$\cdots$	$\cdots$	$\cdots$
Os189	2.9974E-12	4.30E-02	$\cdots$	9.57E-01	$\cdots$	$\cdots$	$\cdots$	$\cdots$	$\cdots$	$\cdots$	$\cdots$
Os190	4.8745E-12	1.40E-01	$\cdots$	8.60E-01	$\cdots$	$\cdots$	$\cdots$	$\cdots$	$\cdots$	$\cdots$	$\cdots$
Os192	7.5705E-12	3.40E-02	$\cdots$	9.66E-01	$\cdots$	$\cdots$	$\cdots$	$\cdots$	$\cdots$	$\cdots$	$\cdots$
Ir191	6.8116E-12	1.90E-02	$\cdots$	9.81E-01	$\cdots$	$\cdots$	$\cdots$	$\cdots$	$\cdots$	$\cdots$	$\cdots$
Ir193	1.1464E-11	1.30E-02	$\cdots$	9.87E-01	$\cdots$	$\cdots$	$\cdots$	$\cdots$	$\cdots$	$\cdots$	$\cdots$
Pt190	4.7599E-15	$\cdots$	$\cdots$	$\cdots$	$\cdots$	1.00	$\cdots$	$\cdots$	$\cdots$	$\cdots$	$\cdots$
Pt192	2.7132E-13	7.92E-01	$\cdots$	$\cdots$	$\cdots$	2.08E-01	$\cdots$	$\cdots$	$\cdots$	$\cdots$	$\cdots$
Pt194	1.1429E-11	6.00E-02	$\cdots$	9.40E-01	$\cdots$	$\cdots$	$\cdots$	$\cdots$	$\cdots$	$\cdots$	$\cdots$
Pt195	1.1728E-11	2.30E-02	$\cdots$	9.77E-01	$\cdots$	$\cdots$	$\cdots$	$\cdots$	$\cdots$	$\cdots$	$\cdots$
Pt196	8.7505E-12	1.21E-01	$\cdots$	8.79E-01	$\cdots$	$\cdots$	$\cdots$	$\cdots$	$\cdots$	$\cdots$	$\cdots$
Pt198	2.4834E-12	$\cdots$	$\cdots$	1.00	$\cdots$	$\cdots$	$\cdots$	$\cdots$	$\cdots$	$\cdots$	$\cdots$
Au197	5.2934E-12	5.90E-02	$\cdots$	9.41E-01	$\cdots$	$\cdots$	$\cdots$	$\cdots$	$\cdots$	$\cdots$	$\cdots$
Hg196	1.9119E-14	$\cdots$	$\cdots$	$\cdots$	$\cdots$	1.00	$\cdots$	$\cdots$	$\cdots$	$\cdots$	$\cdots$

Table 2—Continued

Ion	Solar	Main S	Weak S	R	νP	γ	Ia	Massive	GCR	ν/Novae/GCR	BBN
Hg198	1.2420E-12	1.00	$\cdots$	$\cdots$	$\cdots$	$\cdots$	$\cdots$	$\cdots$	$\cdots$	$\cdots$	$\cdots$
Hg199	2.1024E-12	2.78E-01	$\cdots$	7.22E-01	$\cdots$	$\cdots$	$\cdots$	$\cdots$	$\cdots$	$\cdots$	$\cdots$
Hg200	2.8778E-12	6.75E-01	$\cdots$	3.25E-01	$\cdots$	$\cdots$	$\cdots$	$\cdots$	$\cdots$	$\cdots$	$\cdots$
Hg201	1.6423E-12	5.07E-01	$\cdots$	4.93E-01	$\cdots$	$\cdots$	$\cdots$	$\cdots$	$\cdots$	$\cdots$	$\cdots$
Hg202	3.7209E-12	8.41E-01	$\cdots$	1.59E-01	$\cdots$	$\cdots$	$\cdots$	$\cdots$	$\cdots$	$\cdots$	$\cdots$
Hg204	8.5538E-13	1.02E-01	$\cdots$	8.98E-01	$\cdots$	$\cdots$	$\cdots$	$\cdots$	$\cdots$	$\cdots$	$\cdots$
Tl203	1.4648E-12	7.90E-01	$\cdots$	2.10E-01	$\cdots$	$\cdots$	$\cdots$	$\cdots$	$\cdots$	$\cdots$	$\cdots$
Tl205	3.4967E-12	5.96E-01	$\cdots$	4.04E-01	$\cdots$	$\cdots$	$\cdots$	$\cdots$	$\cdots$	$\cdots$	$\cdots$
Pb204	1.7961E-12	1.00E+00	$\cdots$	$\cdots$	$\cdots$	$\cdots$	$\cdots$	$\cdots$	$\cdots$	$\cdots$	$\cdots$
Pb206	1.6714E-11	6.59E-01	$\cdots$	3.41E-01	$\cdots$	$\cdots$	$\cdots$	$\cdots$	$\cdots$	$\cdots$	$\cdots$
Pb207	1.8496E-11	5.83E-01	$\cdots$	4.17E-01	$\cdots$	$\cdots$	$\cdots$	$\cdots$	$\cdots$	$\cdots$	$\cdots$
Pb208	5.2941E-11	4.23E-01	$\cdots$	5.77E-01	$\cdots$	$\cdots$	$\cdots$	$\cdots$	$\cdots$	$\cdots$	$\cdots$
Bi209	3.7589E-12	5.80E-02	$\cdots$	9.42E-01	$\cdots$	$\cdots$	$\cdots$	$\cdots$	$\cdots$	$\cdots$	$\cdots$
Th232	1.1959E-12	$\cdots$	$\cdots$	1.00	$\cdots$	$\cdots$	$\cdots$	$\cdots$	$\cdots$	$\cdots$	$\cdots$
U234	1.3317E-17	$\cdots$	$\cdots$	1.00	$\cdots$	$\cdots$	$\cdots$	$\cdots$	$\cdots$	$\cdots$	$\cdots$

7.4.   Comparison to Linear Interpolation

Table 3 shows the ratios of the isotopic abundances given by our scaling model over a simple linear interpolation of abundances between BBN and solar. Ratios for all isotopes are given at two different metallicities: [Z]=-1, and [Z]=-3.

Table 2—Continued

Ion	Solar	Main S	Weak S	R	νP	γ	Ia	Massive	GCR	ν/Novae/GCR	BBN
U235	1.5716E-13	$\cdots$	$\cdots$	1.00	$\cdots$	$\cdots$	$\cdots$	$\cdots$	$\cdots$	$\cdots$	$\cdots$
U238	4.8994E-13	$\cdots$	$\cdots$	1.00	$\cdots$	$\cdots$	$\cdots$	$\cdots$	$\cdots$	$\cdots$	$\cdots$

Table 3.   Ratios of Abundances (Scaling Model/Linear Interpolations) at different metallicities

Isotope	[Z]=-1	[Z]=-3	Isotope	[Z]=-1	[Z]=-3	Isotope	[Z]=-1	[Z]=-3
H1	0.9995	1.0000	Mg24	1.0980	1.3675	Ca42	0.6347	0.3899
H2	0.9942	0.9998	Mg25	0.4635	0.1006	Ca43	0.3651	0.0503
He3	1.0088	1.0003	Mg26	0.4644	0.1009	Ca44	0.4238	0.0855
He4	1.0015	1.0001	Al27	0.5634	0.2077	Ca46	0.0097	0.0001
Li6	0.9003	1.0831	Si28	0.7892	0.8704	Ca48	0.0038	0.0000
Li7	0.9530	0.9999	Si29	0.3133	0.0559	Sc45	0.5466	0.1743
Be9	0.9425	1.1584	Si30	0.3129	0.0908	Ti46	0.3777	0.1252
B10	0.9425	1.1584	P31	0.6071	0.3252	Ti47	0.3253	0.0380
B11	0.9425	1.1584	S32	0.9211	1.2657	Ti48	0.5270	0.2676
C12	1.4204	2.9308	S33	0.7507	0.7052	Ti49	0.4319	0.1889
C13	1.5575	3.7785	S34	0.4206	0.1976	Ti50	0.0075	0.0000
N14	0.7076	0.3543	S36	0.0920	0.0026	V50	0.2747	0.0302
N15	0.4852	0.1142	Cl35	0.7423	0.4839	V51	0.4066	0.1976
O16	1.5271	3.6295	Cl37	0.5896	0.2614	Cr50	0.1986	0.1301
O17	0.5994	0.2154	Ar36	0.8476	0.9812	Cr52	0.4000	0.3266
O18	0.0598	0.0002	Ar38	0.4697	0.1978	Cr53	0.2532	0.2076
F19	0.7012	0.3448	Ar40	0.0504	0.0003	Cr54	0.0145	0.0045
Ne20	1.3117	2.2605	K39	0.7738	0.5137	Mn55	0.1331	0.1181
Ne21	0.8830	0.6934	K40	0.8825	0.6874	Fe54	0.0512	0.0759
Ne22	0.2099	0.0232	K41	0.7554	0.4877	Fe56	0.3112	0.3051
Na23	0.7288	0.3911	Ca40	0.6662	0.5927	Fe57	0.7367	0.3999

Table 3—Continued

Isotope	[Z]=-1	[Z]=-3	Isotope	[Z]=-1	[Z]=-3	Isotope	[Z]=-1	[Z]=-3
Fe58	0.0508	0.0037	As75	0.8701	0.8665	Y89	0.5928	0.2084
Co59	0.6743	0.3067	Se74	0.8711	0.8694	Zr90	0.7162	0.5002
Ni58	0.3176	0.0320	Se76	0.5894	0.2048	Zr91	0.6126	0.2552
Ni60	0.8105	0.5328	Se77	0.8948	0.9248	Zr92	0.6423	0.3254
Ni61	0.7482	0.4210	Se78	0.6964	0.4568	Zr94	0.5929	0.2084
Ni62	0.7784	0.4777	Se80	1.0984	1.4044	Zr96	0.8939	0.9206
Ni64	0.1666	0.0574	Se82	1.1529	1.5333	Nb93	0.6392	0.3180
Cu63	0.7444	0.4228	Br79	1.0115	1.1997	Mo92	1.1535	1.5346
Cu65	0.5393	0.1679	Br81	0.8762	0.8808	Mo94	1.1490	1.5240
Zn64	0.7622	0.4474	Kr78	0.8711	0.8694	Mo95	0.7809	0.6532
Zn66	0.4529	0.1032	Kr80	0.6739	0.4042	Mo96	0.5929	0.2084
Zn67	0.3895	0.0946	Kr82	0.6070	0.2453	Mo97	0.8078	0.7169
Zn68	0.3867	0.1117	Kr83	0.9487	1.0517	Mo98	0.7035	0.4702
Zn70	1.1529	1.5333	Kr84	0.9793	1.1234	Mo100	1.1294	1.4776
Ga69	0.7171	0.5062	Kr86	1.0475	1.2840	Ru96	1.1535	1.5346
Ga71	0.5891	0.2044	Rb85	0.8771	0.8825	Ru98	1.1535	1.5346
Ge70	0.5891	0.2044	Rb87	0.9965	1.1633	Ru99	0.9810	1.1266
Ge72	0.7302	0.5370	Sr84	0.8711	0.8694	Ru100	0.5929	0.2084
Ge73	0.7275	0.5305	Sr86	0.5911	0.2066	Ru101	1.0608	1.3154
Ge74	0.7280	0.5315	Sr87	0.5911	0.2065	Ru102	0.8973	0.9286
Ge76	1.1529	1.5333	Sr88	0.5929	0.2084	Ru104	1.1411	1.5054

Table 3—Continued

Isotope	[Z]=-1	[Z]=-3	Isotope	[Z]=-1	[Z]=-3	Isotope	[Z]=-1	[Z]=-3
Rh103	1.0655	1.3264	Sn115	0.5976	0.2134	Xe128	0.5929	0.2084
Pd102	0.7367	0.5438	Sn116	0.5929	0.2084	Xe129	1.1355	1.4922
Pd104	0.5929	0.2084	Sn117	0.8653	0.8530	Xe130	0.5929	0.2084
Pd105	1.0716	1.3410	Sn118	0.7459	0.5705	Xe131	1.1120	1.4365
Pd106	0.8480	0.8119	Sn119	0.8239	0.7548	Xe132	0.9853	1.1368
Pd108	0.7639	0.6129	Sn120	0.7263	0.5241	Xe134	1.1310	1.4816
Pd110	1.1378	1.4975	Sn122	0.9180	0.9776	Xe136	1.1535	1.5346
Ag107	1.0643	1.3238	Sn124	1.1535	1.5346	Cs133	1.0699	1.3370
Ag109	1.0016	1.1752	Sb121	0.9298	1.0055	Ba130	0.5977	0.2136
Cd106	0.5977	0.2136	Sb123	1.1181	1.4511	Ba132	0.5977	0.2136
Cd108	0.5977	0.2135	Te120	0.5977	0.2136	Ba134	0.3097	0.0297
Cd110	0.5929	0.2084	Te122	0.5929	0.2084	Ba135	0.9113	1.1027
Cd111	0.9550	1.0652	Te123	0.5929	0.2084	Ba136	0.3097	0.0297
Cd112	0.7611	0.6063	Te124	0.5929	0.2084	Ba137	0.6126	0.5700
Cd113	0.9281	1.0015	Te125	1.0369	1.2588	Ba138	0.3983	0.1877
Cd114	0.6843	0.4246	Te126	0.9180	0.9776	La138	0.5977	0.2136
Cd116	1.0649	1.3251	Te128	1.1333	1.4869	La139	0.5662	0.4872
In113	0.5977	0.2136	Te130	1.1535	1.5346	Ce136	0.5977	0.2136
In115	0.9242	0.9922	I127	1.1226	1.4617	Ce138	0.5977	0.2136
Sn112	0.5977	0.2136	Xe124	0.5977	0.2136	Ce140	0.4051	0.1998
Sn114	0.5977	0.2136	Xe126	0.5977	0.2136	Ce142	0.9915	1.2457

Table 3—Continued

Isotope	[Z]=-1	[Z]=-3	Isotope	[Z]=-1	[Z]=-3	Isotope	[Z]=-1	[Z]=-3
Pr141	0.7248	0.7701	Gd157	1.0598	1.3676	Yb171	0.9822	1.2291
Nd142	0.3097	0.0297	Gd158	0.9155	1.1102	Yb172	0.7915	0.8890
Nd143	0.8818	1.0500	Gd160	1.1484	1.5256	Yb173	0.9299	1.1358
Nd144	0.7206	0.7626	Tb159	1.0817	1.4067	Yb174	0.6455	0.6287
Nd145	0.9223	1.1223	Dy156	0.5977	0.2136	Yb176	1.0834	1.4097
Nd146	0.6076	0.5609	Dy158	0.5977	0.2136	Lu175	1.0041	1.2682
Nd148	0.9948	1.2517	Dy160	0.3097	0.0297	Lu176	0.3097	0.0297
Nd150	1.1535	1.5346	Dy161	1.1104	1.4579	Hf174	0.5977	0.2136
Sm144	0.5977	0.2136	Dy162	1.0218	1.2999	Hf176	0.3097	0.0297
Sm147	0.9366	1.1479	Dy163	1.1180	1.4714	Hf177	1.0134	1.2848
Sm148	0.3097	0.0297	Dy164	0.9628	1.1945	Hf178	0.6759	0.6828
Sm149	1.0480	1.3465	Ho165	1.0860	1.4142	Hf179	0.8193	0.9387
Sm150	0.3097	0.0297	Er162	0.5977	0.2136	Hf180	0.4304	0.2449
Sm152	0.9619	1.1930	Er164	0.3846	0.0775	Ta180	0.5977	0.2136
Sm154	1.1307	1.4940	Er166	1.0193	1.2953	Ta181	0.7729	0.8559
Eu151	1.1045	1.4473	Er167	1.0767	1.3977	W180	0.5977	0.2136
Eu153	1.1054	1.4488	Er168	0.9096	1.0997	W182	0.6464	0.6302
Gd152	0.3921	0.0823	Er170	1.0497	1.3495	W183	0.6725	0.6768
Gd154	0.3097	0.0297	Tm169	1.0480	1.3465	W184	0.5089	0.3849
Gd155	1.1037	1.4458	Yb168	0.5977	0.2136	W186	0.6692	0.6708
Gd156	1.0058	1.2713	Yb170	0.3097	0.0297	Re185	0.9164	1.1117

Table 3—Continued

Isotope	[Z]=-1	[Z]=-3	Isotope	[Z]=-1	[Z]=-3	Isotope	[Z]=-1	[Z]=-3
Re187	1.0674	1.3811	Pt194	1.1028	1.4443	Tl203	0.4869	0.3457
Os184	0.5977	0.2136	Pt195	1.1340	1.5000	Tl205	0.6506	0.6377
Os186	0.3097	0.0297	Pt196	1.0514	1.3525	Pb204	10	1000
Os187	0.4808	0.1389	Pt198	1.1535	1.5346	Pb206	6.9833	659.52
Os188	0.9130	1.1057	Au197	1.1037	1.4458	Pb207	6.3110	583.64
Os189	1.1172	1.4699	Hg196	0.5977	0.2136	Pb208	4.8955	423.89
Os190	1.0353	1.3239	Hg198	0.3097	0.0297	Bi209	1.6666	59.446
Os192	1.1248	1.4835	Hg199	0.9189	1.1163	Th232	1.1535	1.5346
Ir191	1.1374	1.5060	Hg200	0.5839	0.5188	U234	1.1535	1.5346
Ir193	1.1425	1.5151	Hg201	0.7257	0.7716	U235	1.1535	1.5346
Pt190	0.5977	0.2136	Hg202	0.4439	0.2690	U238	1.1535	1.5346
Pt192	0.3696	0.0680	Hg204	1.0674	1.3811			

REFERENCES

Abia, C., Cunha, K., Cristallo, S., de Laverny, P., Domineguez, I., Eriksson, K., et al., 2010, ApJ, **715**, L94

Arcones, A., & Montes, F., 2011, ApJ, **731**, 5

Arnould, M., & Goriely, S., 2003, Phys. Rep., **384**, 1

Arnould, M., Seiss, L., & Goriely, S., 2003, CNO in the Universe, ASP Conference Series, ed. C. Charbonnel, D. Schaerer, & G. Meynet, Vol. 304

Banerjee, P., Haxton, W., & Qian, Y.-Z., 2011, Phys. Rev. Lett., **106**, 20

Bisterzo, S., Gallino, R., Straniero, O., Cristallo, S., & Käppeler, F., 2010, Mon. Not. R. Astron. Soc., **000**, 1

Bisterzo, S., Gallino, R., et al, 2011, Personal Communication

Bours, M. C. P., Toonen, S., & Nelemans, G., 2013arXiv1302.2629B

Burbidge, M., Burbidge, G., Fowler, W, & Hoyle, F., 1957, Rev. Mod. Phys., **29**, 547

Busso, M., & Gallino, R., 1999, ARA&A, **37**., 239

Cayrel, R, Depagne, E., Spite, M., Hill, V., Spite, F., Francois, P., et al., 2004, A&A, **416**, 1117.

Chiappini, C., Matteucci, F., & Gratton, R., 1997, ApJ, **477**, 765

Clayton, D., & Rassbach, M., 1967, ApJ, **148**, 69

Costa, R., Maciel, W., & Escudero, A., 2009, arXiv:0901.4382v1

Cyburt R., Fields, B., & Olive, K., 2001, New Astronomy **6**, 215-238

Dillmann, I., Plag, R., Käppeler, F., -K., & Rauscher, T., 2009, KADoNIS v0.3, http://www.kadonis.org

Fields, B., 2002. Personal Communication.

Forestini, M., Goriely, S., Jorissen, A., Arnould, M., 1992, A&A, **261**, 157

Frebel, A., 2010, Astronomische Nachrichten, **331**, 474

Frischknecht, U., Hirschi, R., Rauscher, T., & Thielemann, F., 2010, 11th Symposium on Nuclei in the Cosmos, NIC XI

Fröhlich, C., Martï£¡nez-Pinedo, G., Liebendörfer, M., Thielemann, F., Bravo, E., Hix, W., et al., 2006, PRL **96**, 142502

Gallino, R., Arlandini, C., Busso, M., Lugaro, M., Travaglio, C., Straniero, R., et al., 1998, ApJ, **497**, 388

Gehrz, R., Truran, J., Williams, R., & Starrfield, S., 1998, PASP, **110**, 3

Hartmann, D., Haxton, W., Hoffman, R., & Woosley, S., 1991, Nucl. Phys. A **527**, 663

Heger, A. Kolbe, E., Haxton, W., Langanke, K., Martï£¡nez-Pinedo, G., & Woosley, S., 2003, arXiv: astro-ph/0307546v1

Heger, A., Kolbe, E., Haxton, W. C., Langanke, K., Martï£¡nez-Pinedo, G., & Woosley, S., 2005, Phys. Lett. B, **606**, 258

Heger, A., & Woosley, S., 2010, ApJ, **724**, 341

Heil, M., Käppeler, F., Uberseder, E., Gallino, R., & Pignatari, M., 2007, Progress in Particle and Nuclear Physics, **59**, 174

Heil, M., Käppeler, F., Uberseder, E., Gallino, R., Bisterzo, S., & Pignatari, M., 2008, Phys. Rev. C **78**, 025802

Henry, R., Cowan, J., & Sobeck, J., 2010, ApJ, **709**, 715

Hillebrandt, W., & Niemeyer, J., 2000, ARA&A, **38**, 191

Hoffman, R., Woosley, S., & Qian, Y.-Z., 1997, Nucl. Phys. A, **621**, 397

Iben, I., Jr., 1975, ApJ, **196**, 525

Jehin, E., Magain, P., Neuforge, C., Noels, A., Parmentier, G., & Thoul, A., 1999, A&A, **341**, 241

Joggerst, C., & Heger, A., 2008, AIP Conference Proceedings, **990**, 257

José, J., & Hernanz, M., 2007, J. Phys. G: Nucl. Part. Phys., **34**, R431

José, J., & Hernanz, M., 2008, 10th Symposium on Nuclei in the Cosmos

Käppeler, F., Beer, H., & Wisshak, K., 1989, Rep. Prog. Phys. **52**, 945

Käppeler, F., Gallino, R., Bisterzo, S., & Aoki, W., 2011, Rev. Mod. Phys., **83**, 157

Kobayashi, C., Umeda, H., Nomoto, K., Tominaga, N., & Ohkubo, T., 2006, ApJ, **653**, 1145-1171

Lattanzio, J., & Lugaro, M., 2005, arXiv:astro-ph/0505424v1

Lodders, K., 2003, ApJ, **591**, 1220

Lodders, K., Palme, H., & Gail, H.-P., 2009, arXiv:1010.2746v1

Maeda, K., Röpke, F., Fink, M., Hillebrandt, W., Travaglio, C., & Thielemann, F.-K., 2010, ApJ, **712**, 624

Makinaga, A., Utsunomiya, H., Goriely, S., Kaihori, T., Goko, S., Akimune, H., et al., 2009, Phys. Rev. C **79**, 025801

Mannucci, F., Della Valle, M., & Panagia, N., 2006, Mon. Not. R. Astron. Soc. **370**, 773

Martï£¡nez-Pinedo, G., Kelic, A., Langanke, K., Schmidt, K.-H., Mocelj, D., Fröhlich, C., et al., 2006, 9th Symposium on Nuclei in the Cosmos

Mashonkina, L., & Gehren, T., 2001, A&A, **376**, 232

Meneguzzi, M., Audouze, J., & Reeves, H., 1971, A&A, **15**, 337

Meynet, G., & Arnould, M., 2000, A&A, **355**, 176

Ning, H., Qian, Y.-Z., & Meyer, B., 2007, ApJ, **667**, 159

Nomoto, K., Iwamoto, K., Nakasatoa, N., Thielemann, F.-K., Brachwitz, F., Tsujimoto, T., et al., 1997, Nucl. Phys. A, **621**, 467

Pignatari, M., Gallino, R., Meynet, G., Hirschi, R., Herwig, F., & Wiescher M., 2008, ApJ, **687**, L95

Pignatari, M., Gallino, R., Heil, M., Wiescher, M., Käppeler, F., Herwig, F., et al, 2010, ApJ, **710**, 1557

Prantzos, N., 2007, arXiv:astro-ph/0702071v1

Prantzos, N., 2010, Proceedings of the International Astronomical Union, **5** , 473

Prantzos, N., 2011, 11th Symposium on Nuclei in the Cosmos.

Prantzos, N., 2012, A&A, **542**, 67

Qian, Y. -Z., & Wasserburg, G., 2001, ApJ, **559**, 925

Qian, Y. -Z., & Wasserburg, G., 2007, Phys. Rep., **442** 237

Raiteri, C., Gallino, R., Busso, M., Neuberger, D., & Käppeler, F., 1993, ApJ, **419**, 207

Rauscher, T., Heger, A., Hoffman, R., & Woosley, S., 2002, ApJ, **576**, 323-348

Rayet, M., & Prantzos, N., 1990, A&A, **227**, 211

Reeves, H., Fowler, W., & Hoyle, F., 1970, *Nature,* **226**, 727

Soubiran, C., & Girard, P., 2005, A&A, 438, 139-151

Spite, M., Spite, F., 1982, A&A, **115**, 357

Takahashi, K., Yokoi, K., 1987, At. Data Nucl. Data Tables **36**, 375

Taylor, S., Harvin, J., & McAlister, H., 2003, PASP, **115,** 609-617

The Opacity Project Team, *The Opacity Project*, Vol. 1 (1995), Vol. 2 (1996), Institute Of Physics Publishing, Bristol, UK. ISBN 0-7503-0288-7

Thielemann, F.-K., Dillmann, I., Farouqi, K., Fischer, T., Fröhlich, C., Kelic-Heil, A., et al., 2010, Journal of Physics: Conference Series 202, 012006

Timmes, F., Woosley, S., & Weaver, T., 1995, ApJ, **98**, 617-658

Timmes, F., Brown, E., Truran, J., 2003, ApJ, **590**, L83

Ting, Y., Freeman, K., Kobayashi, C., De Silva, G., & Bland-Hawthorn, J., 2012, Mon. Not. R. Astron. Soc. **421**, 1231–1255

Travaglio, C., Galli, D., Gallino, R., Busso, M., Ferrini, F., & Straniero, O., 1999, ApJ, **521**, 691

Travaglio, C., Gallino, R., Arnone, E., Cowan, J., Jordan, F., & Sneden, C., 2004, ApJ, **601**, 864

Travaglio, C., Hillebrandt, W., Reinecke, M., & Thielemann, F.-K., 2004, A&A, **425**, 1029

Truran, J., & Iben, I., Jr., 1977, ApJ, **216**, 797

Truran, J., 1981, A&A, **97**, 391

Truran, J., & Cowan, J., 2000, in Proc. 10th Workshop on Nuclear Astrophysics, ed., W. Hillebrandt & E. Mueller, 64

Truran, J., 2002, in The Physics of Cataclysmic Variables, ASSL, **205**, 453

Tumlinson, J., 2006, ApJ, **641**, 1

Tumlinson, J., 2010, ApJ, **708**, 1398

Tur, C., Heger, A., & Austin, S., 2009, ApJ, **702**, 1068

Walter, G., Beer, H., Käppeler, F., Reffo, G., & Fabbri, F., 1986, A&A, **167**, 186

Woosley, S., & Howard, W., 1978, ApJ Suppl., **36**, 285

Woosley, S., & Haxton, W., 1988, Nature, **334**, 45

Woosley, S., Hartmann, D., , 1990,Hoffman, R., & Haxton, W., ApJ, **356**, 272-301

Woosley, S., 2001, Nucl. Phys. A., **688**, 9

Yao, W.-M., (Particle Data Group), Journal of Physics G 33, 1 (2006)

Yoshida, T., Terasawa, M., Kajino, T., & Sumiyoshi, K., 2004, ApJ, **600**, 204